

See discussions, stats, and author profiles for this publication at: <https://www.researchgate.net/publication/237600505>

# Substructure and superstructure of four-layer Ca-exchanged birnessite

Article in *American Mineralogist* · February 1998

DOI: 10.2138/am-1998-1-210

---

CITATIONS

47

---

READS

952

4 authors, including:



[Bruno Lanson](#)

Université Grenoble Alpes

146 PUBLICATIONS 6,833 CITATIONS

SEE PROFILE

## Substructure and superstructure of four-layer Ca-exchanged birnessite

VICTOR A. DRITS,<sup>1,2</sup> BRUNO LANSON,<sup>2,\*</sup> ANATOLI I. GORSHKOV,<sup>3</sup> AND ALAIN MANCEAU<sup>2</sup>

<sup>1</sup>Geological Institute, Russian Academy of Sciences, 7 Pyzhevsky Street, 109017 Moscow, Russia

<sup>2</sup>Environmental Geochemistry Group, LGIT-IRIGM, BP53, University Joseph Fourier and CNRS, 38041 Grenoble cedex 9, France

<sup>3</sup>Institute of Ore Mineralogy (IGEM), Russian Academy of Sciences, 35 Staromonetny Street, 109017 Moscow, Russia

### ABSTRACT

Synthetic Ca-exchanged birnessite (CaBi) was studied by X-ray and selected-area electron diffraction (XRD, SAED). The substructure of CaBi may be described with a four-layer monoclinic subcell with  $a = 5.150$ ,  $b = 2.844$ ,  $c = 4c' = 28.16$  Å, and  $\beta = 90.3^\circ$ . Two different superstructures of CaBi were distinguished. CaBi type I has cell parameters  $A = 3a = 15.45$ ,  $B = 3b = 8.472$  Å. The stacking sequence in this unit cell may be described as defect-free OSOS, where successive layers are shifted relative to their predecessors by 0 (O) or  $b/2$  (S) along the  $b$  axis. The complete description of stacking involves the structure of the layer itself, the structure of the interlayer, and the shift from this layer to the next one. CaBi type II can be described as a regular interstratification of  $A_p = \frac{3}{2}(a - b)$ ,  $B_p = 4b$ ,  $\gamma = 118.9^\circ$  and  $A_p = \frac{3}{2}(a + b)$ ,  $B_p = -4b$ ,  $\gamma = 118.9^\circ$  supercells that are connected by a mirror plane in projection on the  $a$ - $b$  plane. Its stacking sequence is a random interstratification of OSOS (90%) and OOO (10%) structural fragments. Most CaBi crystals appeared to consist of intergrown type I and type II sub-crystals.

As in Na-rich birnessite, the  $A = 3a$  superstructure arises from the ordered distribution of  $Mn^{3+}$ -rich rows parallel to [010] and separated from each other along [100] by two  $Mn^{4+}$  rows. In  $Mn^{3+}$ -rich rows heterovalent Mn cations are regularly distributed according to  $Mn^{3+}Mn^{3+}Mn^{4+}$  (CaBi type I,  $B = 3b$ ) and  $Mn^{3+}Mn^{3+}Mn^{4+}Mn^{4+}$  (CaBi type II,  $B = 4b$ ) sequences. Super-periodicities along the  $b$  axis are induced by these regular distributions of heterovalent Mn atoms in  $Mn^{3+}$ -rich rows and of associated interlayer Ca. No significant amount of layer vacancies was detected. Idealized structural formulae for CaBi type I and II are  $Ca(Mn_3^{3+}Mn^{4+})O_{18}$  and  $Ca(Mn_3^{3+}Mn_{10}^{4+})O_{24}$ , respectively.

### INTRODUCTION

Buserite and birnessite belong to the family of layered hydrous manganese oxides or phylломanganates. Their layers are built up of edge-shared  $Mn(O,OH)_6$  octahedra. The interlayer space between adjacent layers is occupied by cations and  $H_2O$  molecules. Buserite has a 10 Å periodicity along the  $c^*$  axis with exchangeable cations and two layers of  $H_2O$  molecules in its interlayer space. Partial dehydration of 10 Å buserite leads to the formation of 7 Å birnessite, which has an interlayer space occupied by exchangeable cations and only one  $H_2O$  layer. Birnessite and buserite occur in a wide variety of geological environments such as marine and oceanic Mn nodules (Burns and Burns 1977, 1978; Chukhrov et al. 1978, 1985, 1989; Glover 1977; Drits et al. 1985), terrestrial and oceanic hydrothermal Mn-rich ore deposits (Chukhrov et al. 1987, 1989; Cronan et al. 1982; Dixon and Skinner 1992; Usui et al. 1989; Usui and Mita 1995), and soils (Taylor et al. 1964; Chukhrov and Gorshkov 1981; Chukhrov et al. 1989; Cornell and Giovanoli 1988).

Because of their unique surface charge, redox, and cat-

ion-exchange properties, phylломanganate play an important role in the adsorption and redox processes that occur in various natural environments (McKenzie 1967; Stone and Morgan 1984; Stone and Ulrich 1989; Manceau and Charlet 1992; Stumm 1992; Silvester et al. 1995; Wehrli 1995). To study these cation-exchange properties and the mechanisms of adsorption and redox processes, synthetic buserite and birnessite are used because they are formed easily under laboratory conditions (Bricker 1965; Giovanoli et al. 1970a, 1970b; Murray 1974; Balistrieri and Murray 1982; Strobel et al. 1987; Cornell and Giovanoli 1988) and because they may be considered as synthetic analogs of the natural varieties of these minerals. A comprehensive structural and chemical characterization of these phylломanganate is required to understand these properties and reaction mechanisms at the atomic scale. However at present the structure and crystal chemistry of buserite and birnessite varieties remain incompletely known. There are only a few studies in which fine structural and chemical properties of natural (Chukhrov et al. 1985, 1989; Manceau et al. 1992; Gorshkov et al. 1992) and synthetic (Post and Veblen 1990; Kuma et al. 1994; Drits et al. 1997; Silvester et al. 1997;

\* Author to whom correspondence should be addressed. E-mail: Bruno.Lanson@obs.ujf-grenoble.fr

Manceau et al. 1997) phylломanganates have been investigated. A review of these studies shows that busserite and birnessite structures exhibit some variability. In particular, synthetic birnessite formed under similar physico-chemical conditions but containing different exchangeable cations may have quite different subcells and supercells with contrasting types, amounts, and distributions of stacking faults, structural modulations, and so forth. Each of the birnessite varieties is characterized by specific layer stacks and spatial distributions of heterovalent  $Mn_{\text{layer}}$  cations, as well as by specific distributions of interlayer cations and layer vacancies. Because these characteristics determine its adsorption and redox properties, each birnessite variety containing a given interlayer cation and formed under defined physico-chemical conditions requires a comprehensive structural and crystal-chemical characterization.

This paper describes the structure of synthetic Ca-exchanged birnessite. Despite the fact that natural Ca-rich birnessite (Chukhrov et al. 1979, 1989) and synthetic Ca-exchanged birnessite (Kuma et al. 1994) have been studied by diffraction methods, even the position of Ca in the subcell interlayer of this variety remains uncertain; the origin of the supercell is also subject to discussion. It is shown in this paper that Ca-exchanged birnessite, hereafter referred to as CaBi, is characterized by a set of remarkable structural and chemical features that distinguish this variety from those described in the literature. Only the combined use of selected-area electron diffraction (SAED) and simulation of the diffraction effects from various types of models and stacking faults made possible the correct interpretation of the experimental data, characterized by a non-rational series of  $hkl$  reflections and by contrasting reflection intensities within the same angular domain. The methodology used to obtain these results is detailed.

## PREVIOUS STRUCTURAL STUDIES

### Birnessite with hexagonal unit cells

Buser and Graf (1955), Giovanoli et al. (1970a), Burns and Burns (1977), Chukhrov et al. (1978), and Giovanoli and Arrhenius (1988) proposed a birnessite structure analogous to that of chalcophanite ( $ZnMn_3O_7 \cdot 3H_2O$ ; Wadsley 1955; Post and Appleman 1988). They assumed that birnessite layers have vacancies and interlayer cations located above or below vacant octahedra, and a vacancy model for hydrous phylломanganates has been developed by Strobel et al. (1987). All these models were based on intuitive considerations without a quantitative analysis of X-ray diffraction (XRD) patterns. Chukhrov et al. (1985) presented the first structural study of natural birnessite based on the comparison between experimental and calculated XRD patterns. It was concluded that the sample under study had a one-layer hexagonal unit cell, with its layer containing vacancies and interlayer cations located above or below vacant octahedra. The existence of corner linkages between layer and interlayer cations in this sam-

ple was then confirmed by X-ray absorption spectroscopy (Manceau et al. 1992). Synthetic one-layer hexagonal birnessite samples obtained at low pH (Giovanoli et al. 1976; Glover 1977; Drits et al. 1997) were considered as analogs of natural hexagonal birnessite by Drits et al. (1997). Their results confirmed the similarity between one-layer hexagonal birnessite and three-layer rhombohedral chalcophanite structures.

### Birnessite with monoclinic unit cells

In contrast to hexagonal birnessite, monoclinic birnessite samples are synthesized at high pH and contain exchangeable cations such as  $Na^+$ ,  $Mg^{2+}$ , and  $K^+$ . Their substructure was determined for the first time by Post and Veblen (1990) using the Rietveld technique. These birnessite samples had one-layer monoclinic subcells, the shape and size of which varied with the nature of interlayer cations. The layers of studied varieties did not contain a significant number of vacant octahedra. The structure and crystal chemistry of synthetic Na-rich busserite and Na-rich birnessite, hereafter referred to as NaBu and NaBi, respectively, as well as their transformation mechanism were further studied by Drits et al. (1997) and Silvester et al. (1997) using XRD, SAED, and extended X-ray absorption fine structure spectroscopy (EXAFS). The results obtained by these authors may be summarized as follows: A 10 Å NaBu sample synthesized at high pH consisted of vacancy-free layers and was characterized by the composition  $Na_{0.30}(Mn_{0.69}^{4+}, Mn_{0.31}^{3+})O_{-2}$  and a one-layer monoclinic unit cell ( $a = 5.223$ ,  $b = 2.854$ ,  $c = 10.265$  Å, and  $\beta = 98.6^\circ$ ). NaBu layers had an orthogonal symmetry ( $\% \neq \sqrt{3}$ ). The departure from the orthogonal symmetry resulted from the unique azimuthal orientation of Jahn-Teller distorted  $Mn^{3+}$  octahedra. Partial dehydration of NaBu lead to the formation of the one-layer monoclinic structure of NaBi having a subcell with  $a = 5.175$ ,  $b = 2.850$ ,  $c = 7.342$  Å, and  $\beta = 103.2^\circ$  and the composition  $Na_{0.30}Mn_{0.05}^{2+}(Mn_{0.74}^{4+}, Mn_{0.21}^{3+}, \square_{0.05})O_{-2}$ . NaBi also had an orthogonal layer symmetry.  $Mn^{3+}$  cations in NaBu and NaBi layers were segregated in rows parallel to [010] and separated from each other along [100] by two  $Mn^{4+}$  rows to minimize strains because of the Jahn-Teller distortion of  $Mn^{3+}$  octahedra. This ordered distribution of  $Mn^{4+}$  and  $Mn^{3+}$  cations gave rise to the superstructure with  $A = 3a$ .

The transformation of NaBu into NaBi was accompanied by the formation of a certain amount of  $Mn^{2+}$  cations because of disproportionation according to  $Mn_{\text{layer}}^{3+} + Mn_{\text{layer}}^{3+} \rightarrow Mn_{\text{layer}}^{4+} + Mn_{\text{interlayer}}^{2+}$ . This reaction took place within  $Mn^{3+}$ -rich rows and the newly formed  $Mn_{\text{layer}}^{4+}$  and  $Mn_{\text{interlayer}}^{2+}$  were distributed periodically along the  $b$  axis.  $Mn^{2+}$  migrated in the interlayer region leading to the formation of layer vacancies (Silvester et al. 1997). The supercell with  $A = 3a$  and  $B = 6b$  contained two  $Mn^{2+}$  atoms and two vacancies per 36 octahedra (Drits et al. 1997).

### Origin of the superstructures

One of the interesting problems in the crystal chemistry of birnessite is the origin of superstructures because

two main interpretations have been proposed in the literature. Giovanoli et al. (1970a) were the first to observe the existence of superreflections in the SAED patterns of NaBi and related these superstructures to an ordered distribution of layer vacancies. This hypothesis was also supported by Chukhrov et al. (1978, 1979, 1989) from the SAED study of a natural Ca-rich birnessite sample in which they distinguished two phases called "14 Å Ca-birnessite and clinobirnessites". The "14 Å Ca-birnessite" particles were described by the supercell parameters  $A = 3a = 15.33$ ,  $B = 3b = 8.52$  Å,  $c = 14.39$  Å  $\gamma = 90^\circ$ . SAED patterns of "Ca-clinobirnessite" particles also contained superreflections that were distributed with an oblique layer supercell ( $a = 10.44$ ,  $b = 8.70$ ,  $c = 7$  Å  $\gamma = 110^\circ$ ).

More recently, Kuma et al. (1994) studied a large collection of synthetic busserite and birnessite samples containing various interlayer cations ( $\text{Na}^+$ ,  $\text{K}^+$ ,  $\text{Cs}^+$ ,  $\text{Ca}^{2+}$ ,  $\text{Mg}^{2+}$ ,  $\text{Sr}^{2+}$ , ...) and concluded that interlayer cations were located above or below vacant sites that were regularly distributed along the  $b$  axis of the layers. The vacancy-rich rows were separated by two complete rows of Mn octahedra leading to the  $A = 3a$  super-periodicity. For the birnessite samples containing Mg-, Ca-, Sr-, Ba-, and Ni, additional "characteristic" superreflections were observed and related to an ordered distribution of interlayer cations. These additional super-periodicities varied as a function of the nature and of the amount of exchanged cations.

This interpretation of the SAED superreflections in terms of ordered vacancy distribution contradicted the experimental data obtained by XRD (Post and Veblen 1990; Drits et al. 1997) and EXAFS (Manceau et al. 1992; Silvester et al. 1997) techniques. According to these data, one-layer hexagonal birnessite has a large amount of layer vacancies but their SAED patterns did not contain, or contained extremely weak, superreflections (Chukhrov et al. 1985, 1989; Drits et al. 1997). On the contrary, one-layer monoclinic birnessite synthesized at high pH was characterized by almost vacancy-free layers, and their SAED patterns did contain superreflections, the distribution of which mainly depended on the nature of interlayer cations and on the layer charge, that is on the  $\text{Mn}^{3+}:\text{Mn}^{4+}$  ratio and on the amount of vacancies in  $\text{Mn}^{3+}$ -rich rows. From the analysis of XRD and SAED data, Post and Veblen (1990) concluded that in monoclinic varieties superreflections were likely to result from a regular distribution of interlayer cations. This conclusion was also supported by Manceau et al. (1992), Drits et al. (1997), and Silvester et al. (1997).

### EXPERIMENTAL PROCEDURES

The synthetic CaBi sample was prepared by shaking an NaBu suspension ( $40 \text{ g/dm}^3$ ) in a  $\text{Ca}(\text{NO}_3)_2$  solution ( $1.0 \text{ mol/dm}^3$ ). After equilibrating the cation exchange reaction for 24 h (final pH  $\approx 9-10$ ), the solid was filtered and dried yielding CaBi. The initial NaBu suspension was formed by the oxidation, with bubbling  $\text{O}_2$ , of freshly

precipitated  $\text{Mn}(\text{OH})_2$  suspension in aqueous NaOH (pH  $\approx 9-10$ ; Giovanoli et al. 1970a). Powder XRD patterns were obtained using  $\text{CoK}\alpha$  radiation with a Siemens D5000 powder diffractometer equipped with a Kevex Si(Li) solid-state detector. Intensities were measured at intervals of  $0.04^\circ 2\theta$  with a 30 s counting time per step. Accuracy of  $2\theta$  position was better than  $0.001^\circ$ . SAED patterns were recorded using a JEM-100C microscope operated at 100 kV and equipped with a Kevex spectrometer and a tilting sample holder, after deposition of diluted CaBi suspension on carbon-coated copper grids. The technique used for the interpretation of SAED patterns is described by Drits (1987). After dissolution of the CaBi suspension in an  $\text{HONH}_2\text{Cl}$  (10%) and  $\text{HNO}_3$  (1%) solution, Mn was analyzed by atomic absorption and Ca and Na by ICP analysis. The molar ratios Ca/Mn and Na/Mn were 0.111 and 0.025, respectively. One may note that the Ca/Mn ratio determined for our CaBi sample is identical to the one determined by Kuma et al. (1994).

### SIMULATION OF XRD PATTERNS

The presence of stacking faults often prevents crystal-chemical study of phyllosulfates by conventional methods of structural analysis, including the Rietveld method. One of the only effective ways to obtain structural and crystal-chemical information from such minerals is to simulate diffraction effects from realistic structural models and then compare calculated and experimental XRD patterns (Drits and Tchoubar 1990). The actual crystal structure is determined by a trial-and-error fitting procedure. This approach was applied successfully to natural and synthetic one-layer hexagonal birnessite (Chukhrov et al. 1985; Manceau et al. 1997). To simulate diffraction effects for structural models of CaBi we used a program written by Alain Plançon at the University of Orléans. It is based on the mathematical formalism described by Plançon (1981), Sakharov et al. (1982a, 1982b) and in more detail by Drits and Tchoubar (1990). This program permits us to calculate XRD patterns from models containing random stacking faults as well as stacking faults caused by the fluctuation of layer positions along  $a$ ,  $b$ , or both directions (which are random only with respect to translation in specified directions). For these calculations, coherent scattering domains (CSD) in the layer plane have a disk-like shape with a radius determined by fitting the 200 reflection. The CSD size distribution along the  $c$  axis was quantified by two parameters: the average ( $N_{\text{mean}}$ ) and maximum ( $N_{\text{max}}$ ) number of layers (Reynolds 1989).

### RESULTS

#### Indexing of the experimental XRD pattern in terms of a one-layer subcell

The powder XRD pattern of the sample under study (Fig. 1) contains a set of basal reflections with  $d$  values that correspond to a minimum periodicity along  $c$  equal to  $7.04$  Å. In the  $75-80^\circ 2\theta$  ( $\text{CoK}\alpha$ ) region, two reflections with  $d = 1.412$  Å and  $d = 1.424$  Å were ob-

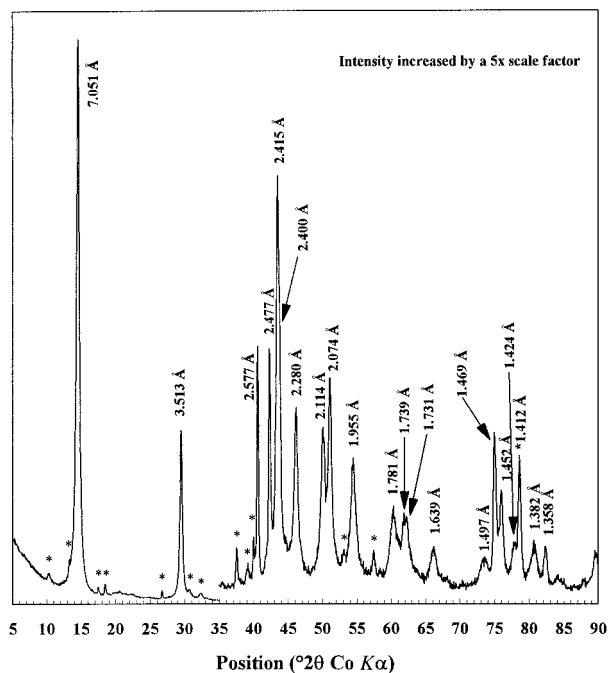


FIGURE 1. Experimental XRD pattern of CaBi. Major diffraction lines are labeled with their positions. Additional lines, related to supercells, are marked with an asterisk.

served in the region where the 020 reflection was expected (Post and Veblen 1990; Chukhrov et al. 1985). According to the literature, XRD patterns of all studied birnessite and busenite samples, both synthetic and natural, may be indexed in terms of a one-layer subcell, hexagonal or monoclinic (Chukhrov et al. 1985; Post and Veblen 1990; Kuma et al. 1994; Manceau et al. 1997). However all attempts to find a unique one-layer unit cell describing the positions of all observed reflections (Fig. 1) failed, and we had to consider the possibility of a mixture of two modifications with different subcells. Subcell I has  $a = 5.150$ ,  $b = 2.848$ ,  $c = 7.040$  Å, and  $\beta = 90.3^\circ$  whereas subcell II has  $a = 5.150$ ,  $b = 2.848$ ,  $c = 7.144$  Å, and  $\beta = 99.8^\circ$ . Table 1 compares  $d_{\text{cal}}(hkl)$  values calculated for each subcell with experimental  $d_{\text{exp}}(hkl)$ . The difference between  $d_{\text{cal}}(hkl)$  and  $d_{\text{exp}}(hkl)$  exceeds 0.003 Å only for one reflection (110, subcell II) and on average is equal to  $\pm 0.001$  Å. Note that the reflections of subcell I with 111 indices are missing, whereas subcell II does not show reflections with 20l indices (Table 1).

### Selected-area electron diffraction

The main types of SAED patterns observed for CaBi crystals are shown in Figures 2a, 3a, 4a, and 5. SAED patterns shown in Figures 2a, 3a, 4a, and 5a are referred to here as CaBi types I, II, III, and IV, respectively. All these patterns contain a set of strong  $hk0$  reflections distributed according to a pseudo-hexagonal orthogonal symmetry. The  $a/b$  ratios determined from experimental SAED patterns are different for the different varieties.

TABLE 1. Indexing of the experimental XRD pattern of CaBi with two subcells

Experimental $d_{\text{exp}}(hkl)$	Subcell I		Subcell II	
	$hkl$	$d_{\text{cal}}(hkl)$	$hkl$	$d_{\text{cal}}(hkl)$
9.941*				
7.703*				
7.051	001	7.040	001	7.040
5.865*				
5.554*				
3.866*				
3.513	002	3.520	002	3.520
3.378*				
3.210*				
2.778*				
2.669*				
2.615*				
2.577	200	2.575		
2.477			110	2.484
2.415	201	2.414		
2.400 (s)			11 $\bar{1}$	2.406
2.280			11 $\bar{1}$	2.283
2.114			11 $\bar{2}$	2.114
2.074	202	2.073		
2.000*				
1.955			112	1.954
1.860*				
1.781			11 $\bar{3}$	1.781
1.739	20 $\bar{3}$	1.739		
1.731	203	1.730		
1.639			11 $\bar{3}$	1.639
1.497			114	1.496
1.469	310	1.470		
1.452	204	1.449		
1.424	020	1.424	020	1.424
1.412*				
1.382			114	1.383
1.358	31 $\bar{2}$	1.359		
1.335				
1.290				
1.270			11 $\bar{5}$	1.271
1.268				

Note:  $a = 5.150$ ,  $b = 2.848$ ,  $c = 7.040$  Å, and  $\beta = 90.3^\circ$  (subcell I) and  $a = 5.150$ ,  $b = 2.848$ ,  $c = 7.144$  Å, and  $\beta = 99.8^\circ$  (subcell II). Calculated  $d_{\text{cal}}(hkl)$  reflection positions are compared to experimental  $d_{\text{exp}}(hkl)$  ones. (s) indicates that the 2.400 Å line is a shoulder difficult to index accurately.  $b$  parameter of subcell I is approximate as no 111 lines are observed experimentally for this subcell.

\* Indicates additional lines related to supercells.

These ratios are equal to 1.835, 1.806, 1.820, and 1.808 for birnessite types I–IV, respectively. Since the  $a$  parameters are similar (5.15 Å) for the two subcells identified by XRD, the two possible  $b$  parameters deduced from XRD data (2.824 and 2.848 Å) have been attributed to CaBi type I and II, respectively, as a function of their  $a/b$  ratio. CaBi type III is assumed to have a  $b$  parameter intermediate between those of CaBi type I and II. It is difficult to estimate the error introduced to these axial ratios by the possible misorientation of the microcrystals with respect to the electron beam. However, the  $a/b$  ratios determined from different microcrystals for the various types of CaBi are very consistent and suggest that (001) planes of the crystals were almost ideally perpendicular to the beam. Relative error in the distances between reflections located along the  $a^*$  and the  $b^*$  axes is estimated to be about 0.1%. Along with the strong subcell reflections, the diffraction patterns contain weaker reflections

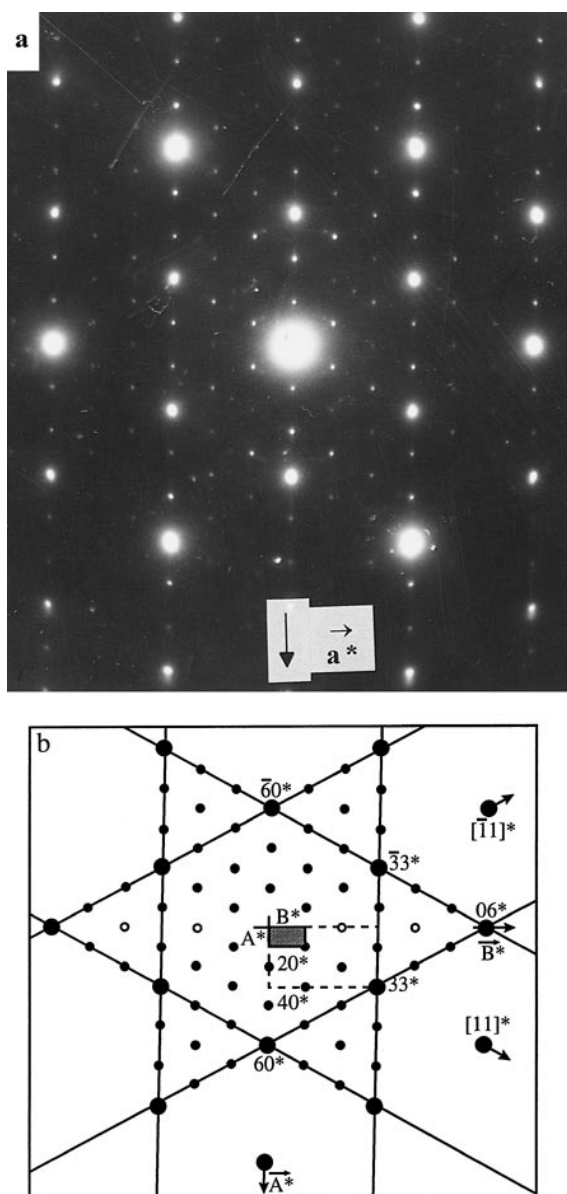


**FIGURE 2.** Observed (a) and schematic (b) SAED patterns of CaBi type I. The experimental pattern is collected with the electron beam normal to the basal surface of the crystal. Reflections from the subcell are shown as large solid circles. Reflections from the supercell are shown as small circles. Empty circles show faint reflections. The supercell is shown as a gray rectangle. The dashed line outlines the subcell.

arising from superstructures that are different for the different CaBi varieties.

**CaBi type I.** As can be seen in Figure 2, the space between two neighboring subcell reflections is divided into three equal parts by two superreflections. The total distribution of  $hk0$  reflections may be described, in reciprocal space, by a supercell with  $A^* = a^*/3$ ,  $B^* = b^*/3$ , and  $\gamma^* = 90^\circ$  parameters, corresponding to  $A = 3a = 15.45$ ,  $B = 3b = 8.472$  Å, and  $\gamma = 90^\circ$  in direct space.

**CaBi type II.** To interpret this supercell reflection distribution it was necessary to assume that the CaBi crystals are twinned. The SAED pattern in Figure 3a can then be considered as the sum of two patterns rotated with respect to each other by  $180^\circ$  around the  $a^*$  axis. The superreflection distributions of one twin component and of the sum of both twins are schematically shown in Figures 3b and 3c, respectively. As can be seen in Figure 3b the distribution of superreflections of each twin component may be described by the oblique supercell with

$$A_p^* = 2a^*/3, \quad B_p^* = (a^* + b^*)/4,$$

$$\gamma^* = 61.1^\circ \text{ corresponding to the supercell}$$

$$A = \frac{3}{2}\sqrt{a^2 + b^2} = 8.828 \text{ \AA},$$

$$B = 4b = 11.392 \text{ \AA}, \quad \gamma = 118.9^\circ.$$

SAED patterns obtained from CaBi type II crystals always consisted of the two overlapped and twinned networks of superreflections; SAED patterns containing only one of the superreflection networks were never observed. Furthermore, superreflections having the same indices and belonging to the two networks always had identical intensities. It should be emphasized that the same features are observed in SAED patterns of natural (Chukhrov et al. 1979) and synthetic (Gorshkov et al. 1992; Kuma et al. 1994) CaBi. It is unlikely that every single CaBi type II microcrystal consists of two twinned subcrystals having identical thicknesses. The twinning is very fine to give the equal intensities systematically observed for both sets of twins. Therefore it is more likely that CaBi type II consists of right-hand and left-hand structural fragments forming a regularly interstratified structure. Figure 3c shows that all superreflections observed in the SAED patterns of CaBi type II may be described in terms of a unique supercell ( $A^* = a^*/12$ ,  $B^* = b^*/4$ , and  $\gamma^* = 90^\circ$ ), corresponding to the  $A = 12a = 61.80$ ,  $B = 4b = 11.392$  Å,  $\gamma = 90^\circ$  supercell in real space. However it is not clear whether this supercell corresponds to the actual crystal structure of CaBi type II or if it simply describes the coincidence of the twinned reciprocal lattice nodes. Additional sections of the reciprocal lattice of CaBi type II microcrystals should be obtained to solve this problem unambiguously. As a consequence, the oblique primitive supercells are used to describe CaBi type II. The orientations of these two supercells are connected by a mirror plane in projection on the  $a$ - $b$  plane. Additionally, one may note that the primitive supercells have a periodicity equal to  $A \sin \gamma = 3a/2$  along the  $a$  axis.

**CaBi type III.** The SAED pattern shown in Figure 4a represents two overlapped networks of CaBi type I and II superreflections (Fig. 4b). For this variety, the  $a/b$  ratio (1.820) determined from SAED patterns is intermediate between those of CaBi type I and II (1.835 and 1.806, respectively). As a consequence, an intermediate  $b$  parameter (2.844 Å) has been used for the supercell dimensions. Accordingly, the two superreflection networks ob-

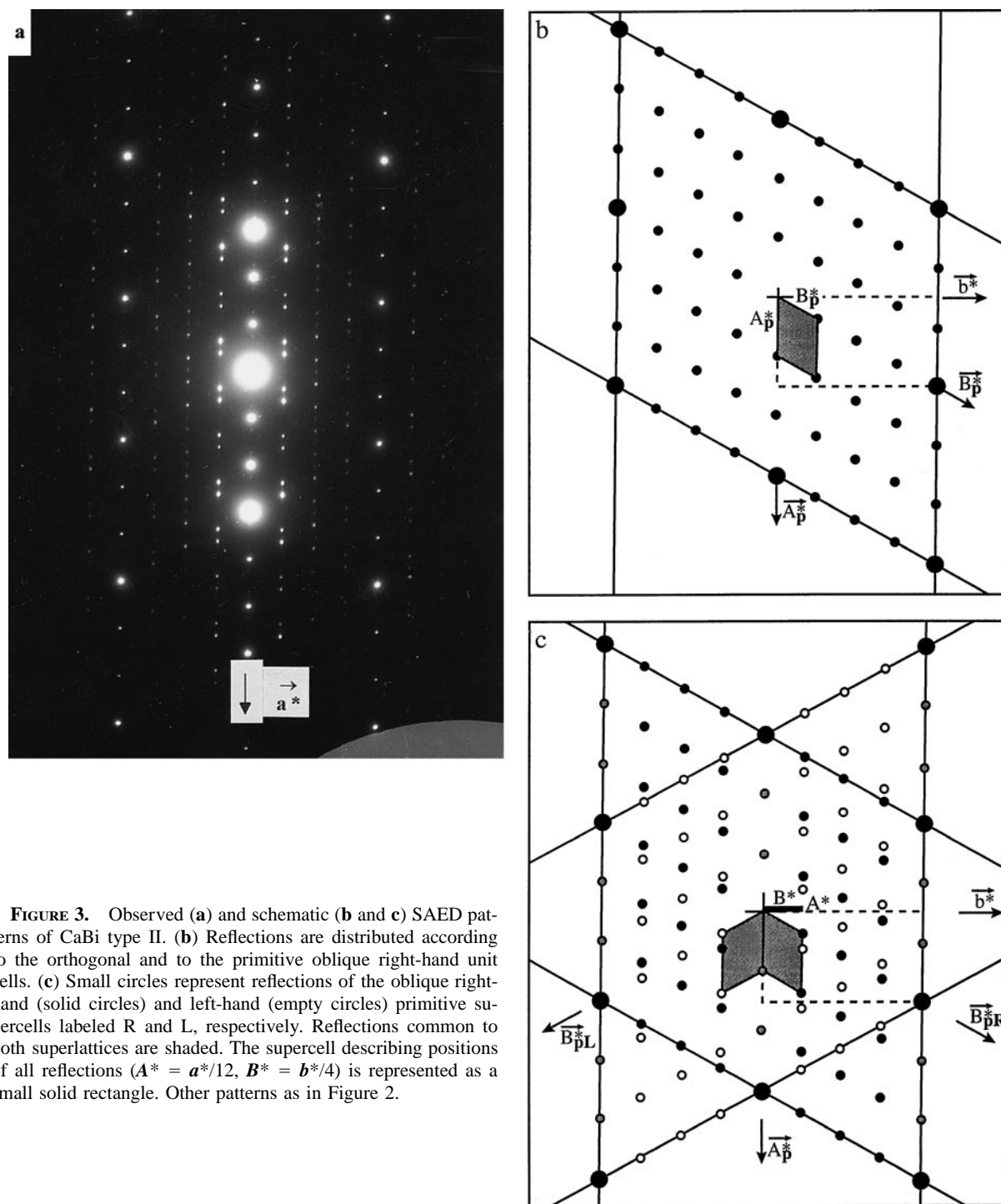


**FIGURE 3.** Observed (a) and schematic (b and c) SAED patterns of CaBi type II. (b) Reflections are distributed according to the orthogonal and to the primitive oblique right-hand unit cells. (c) Small circles represent reflections of the oblique right-hand (solid circles) and left-hand (empty circles) primitive supercells labeled R and L, respectively. Reflections common to both superlattices are shaded. The supercell describing positions of all reflections ( $A^* = a^*/12$ ,  $B^* = b^*/4$ ) is represented as a small solid rectangle. Other patterns as in Figure 2.

served in Figure 4 correspond, in real space, to two supercells with  $A = 3a = 15.45$ ,  $B = 3b = 8.532$  Å, and  $\gamma = 90^\circ$ , and  $A = \frac{3}{2}\sqrt{a^2 + b^2} = 8.825$  Å,  $B = 4b = 11.376$  Å, and  $\gamma = 118.9^\circ$ , respectively. Additionally, it was observed that SAED patterns obtained for different CaBi type III crystals differ from each other by the intensity ratio of the two different networks.

**CaBi type IV.** The SAED pattern shown in Figure 5a represents the sum of two SAED patterns of birnessite type II that are rotated by  $120^\circ$  with respect to each other. The corresponding CaBi type IV crystals consist of two intergrown CaBi type II subcrystals rotated around the  $c^*$  axis by  $120^\circ$ . Figure 5b shows two different diffraction patterns obtained from the external parts of such a crystal.

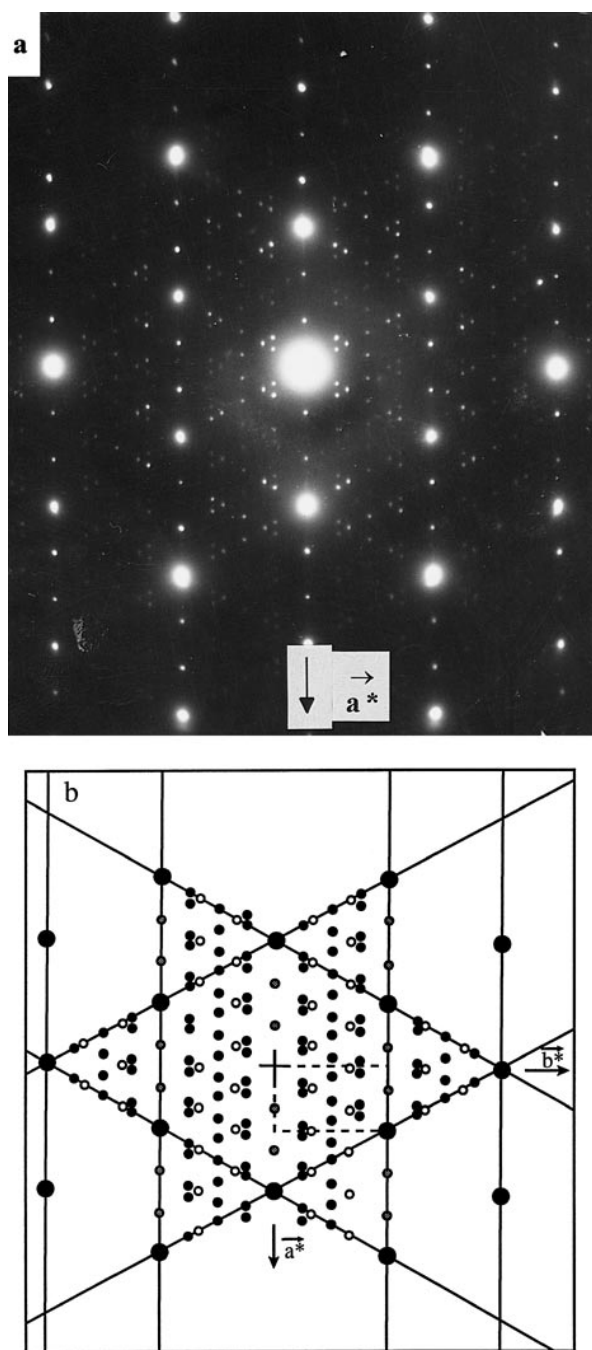


FIGURE 4. Observed (a) and schematic (b) SAED patterns of CaBi type III that represents the sum of the SAED patterns obtained for CaBi type I (empty circles) and CaBi type II (solid circles). Reflections common to both superlattices are shaded. Other patterns as in Figure 2.

The overlap of these subcrystals gives rise to the SAED pattern shown in Figure 5a. There is no lattice accommodation between the two intergrown subcrystals.

Finally, it must be emphasized that types III and IV are not distinct superstructures in the same sense as types

I and II. Type III is a coherent intergrowth of types I and II, whereas type IV is twinned type II.

#### Structural models for one-layer subcells

In agreement with previous experimental data (Post and Veblen 1990; Manceau et al. 1992; Drits et al. 1997; Silvester et al. 1997) we assumed that busserite and birnessite synthesized under high pH conditions consisted of Mn layers without significant numbers of vacancies. Since  $C$ -centered subcell parameters are known, the unique variable parameter for  $Mn_{\text{layer}}$  and  $O_{\text{layer}}$  atomic positions is layer thickness. As a first approximation we assumed that the thickness of Mn layers in CaBi varieties was similar to that determined in NaBi, that is around 1.90–2.00 Å (Post and Veblen 1990). Once general agreement between calculated and experimental XRD patterns had been obtained, this parameter could be refined. Because the mutual arrangement of adjacent layers is also unambiguously determined by the subcell parameters, the main remaining problem is the determination of site position and occupancy for Ca and  $H_2O$  within the interlayer space for subcells I and II. For the calculation of XRD patterns corresponding to the various structural models, a vacancy-free layer was used as a starting point, whereas the amount of Ca and was adjusted to 0.11 and 0.6, respectively, per octahedron. This amount of Ca is in good agreement with the chemical composition determined for this sample as well as with the data obtained by Kuma et al. (1994) for Ca-exchanged busserite.

**Subcell I.** Figure 6a shows the mutual arrangement of atoms defining the interlayer region when adjacent layers are displaced, with respect to each other, by  $c \cdot \cos \beta = -0.007a$  along the  $a$  axis. As can be seen in Figure 6a, four different models may be drawn for Ca positions. The atomic coordinates for Mn, O, Ca, and  $H_2O$  of each model are given in Table 2a.  $H_2O$  positions were chosen that provided octahedral coordination for Ca, with average Ca- $H_2O$  distances around 2.45–2.55 Å. For three of these models (1, 3, and 4) Ca is located in the middle (along the  $c^*$  axis) of the interlayer space. To provide acceptable Ca-O distances in model 2, Ca is shifted toward the center of the tridentate cavity located above (Fig. 6a) or below. Model 4 seems unattractive because Mn of adjacent layers and interlayer Ca are all positioned along the same line parallel to the  $c^*$  axis, which would lead to unjustified strong electrostatic interaction between these cations. Simulation of XRD patterns showed that none of the four models reproduces correctly the experimental XRD pattern. However it was found that for model 1 the distribution of calculated intensities for  $20l$  reflections is similar to the observed one (Fig. 7a) but the calculated pattern contains in addition very strong  $11l$  reflections along with  $20l$  ones (Fig. 7b). If a considerable number of stacking faults are introduced because of displacements of layers along the  $b$  axis, then agreement between simulated and experimental XRD profiles is much better. However introduction of this type of defect in model 1



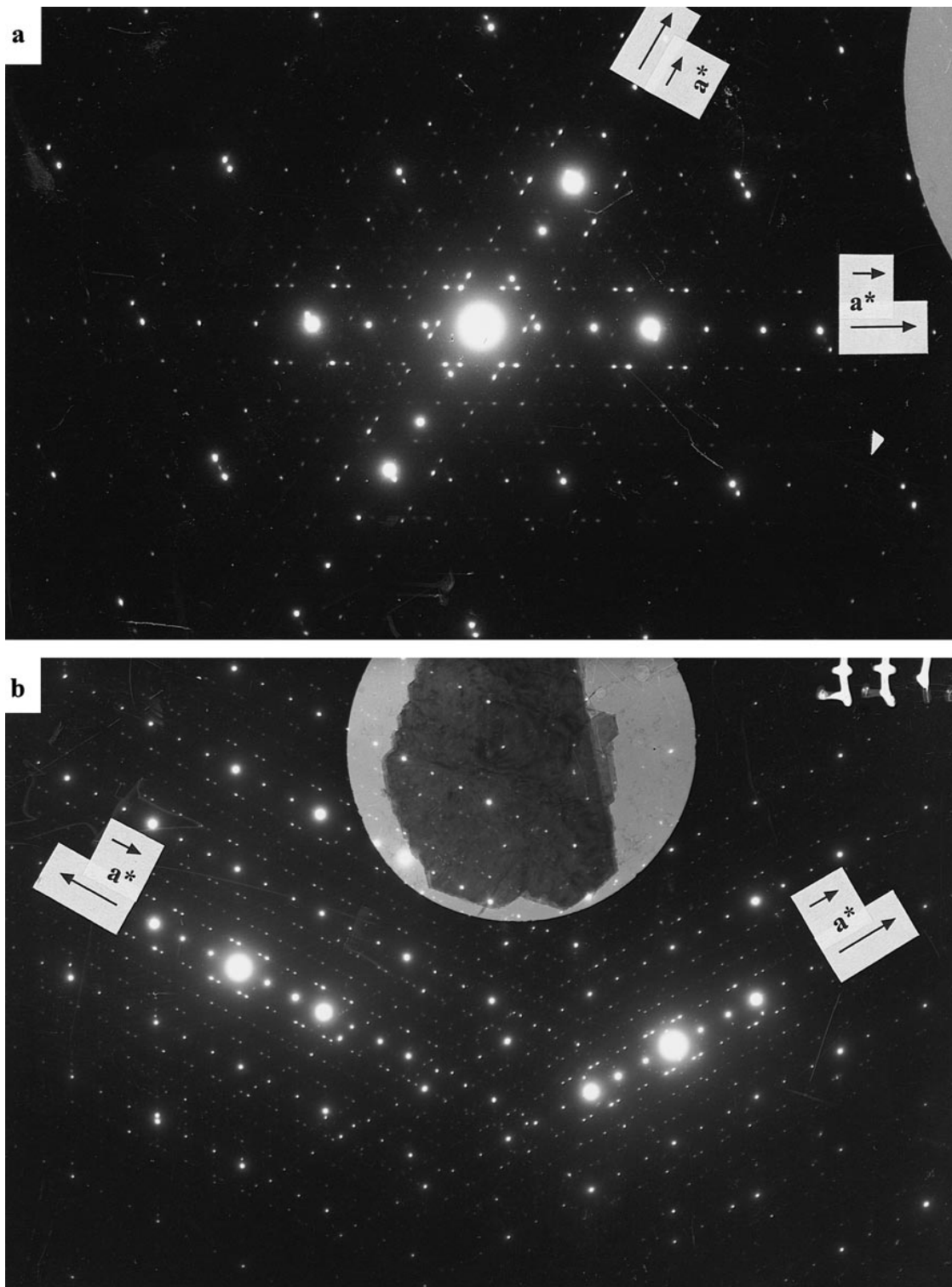


**FIGURE 5.** (a) Observed SAED patterns of CaBi type IV that represents the sum of two SAED patterns of CaBi type II rotated by  $120^\circ$  with respect to each other. The two diffraction patterns obtained from the external parts of the crystal are shown in (b).

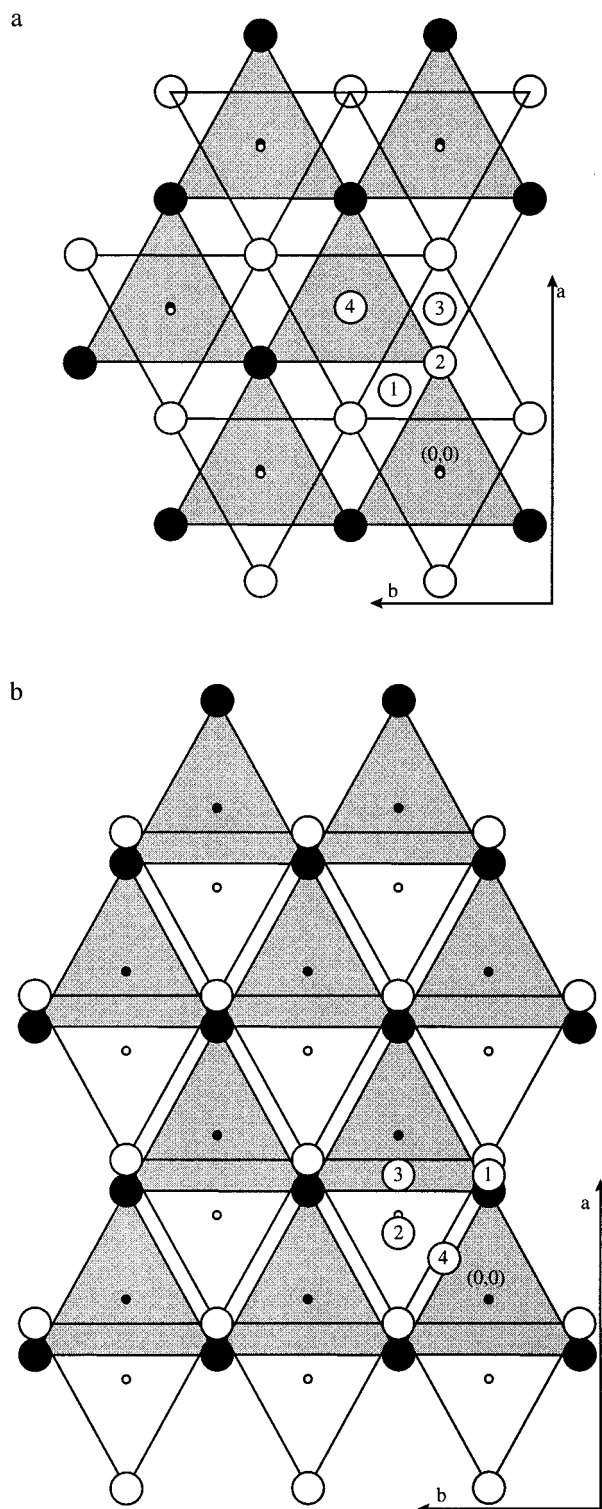


**FIGURE 6.** (a) Possible positions of Ca in the interlayer space of CaBi subcell I. Adjacent layers are translated by  $c \cdot \cos \beta = -0.007a$  along the  $a$  axis. Small black and white circles correspond to Mn cations of lower and upper, respectively, adjacent layers defining the interlayer space. O atoms forming the upper surface of the lower layer (shaded triangles) are shown as large black circles. O atoms forming the lower surface of the upper layer (empty triangles) are shown as large open circles. The circles containing numbers indicate possible positions for Ca; these numbers refer to a defined model. Positions of  $H_2O$  molecules are omitted. (b) Possible positions of Ca in the interlayer space of CaBi subcell II. Adjacent layers are translated by  $c \cdot \cos \beta = -0.236a$  along the  $a$  axis. Symbols and notations as in Figure 6a.

ers are displaced, with respect to each other, by  $c \cdot \cos \beta = -0.236a$  along the  $a$  axis. Among the four possible models shown in Figure 6b and described quantitatively in Table 2b, models 3 and 4 seem unattractive because calculated Ca-O distances are too large from a crystal chemical point of view. In model 2, Ca has a distorted prismatic coordination and should be shifted, along the  $c^*$  axis, toward the center of the tridentate cavity located above or below (Fig. 6b) to get more acceptable Ca-O distances. The local environment of Ca in model 1 is similar to that in model 1 (subcell I), which is coordinated by one O atom from each layer (Fig. 6a). However none of the XRD patterns calculated for models 1–4 led to agreement with the experimental pattern.

In conclusion, even though the indexing of the experimental XRD pattern in terms of two one-layer unit cells is realistic, it is impossible with such a model to obtain a distribution of intensities consistent with the experimental one. In the following section indexing of the experimental XRD pattern in terms of a multilayer unit cell is considered.

#### Indexing of the experimental XRD pattern in terms of multi-layer subcell

As derived from the SAED data, the sample under study is a mixture of three varieties that may all be described by a  $C$ -centered layer subcell. Because the  $a$  values found for subcells I and II are identical (5.150 Å), this parameter can be fixed. A slight variation of the  $b$  parameter should not strongly influence the general result of indexing. The only variable parameters are  $c$  and  $\alpha$  if the  $\beta$  values found for the one-layer subcells are used. All attempts to index the experimental XRD pattern with  $\beta = 99.8^\circ$ , determined for subcell II, failed; however, all strong reflections were successfully indexed with a four-layer  $C$ -centered monoclinic subcell with  $a = 5.150$ ,  $b = 2.844$ ,  $c = 4c' = 28.16$  Å, and  $\beta = 90.3^\circ$  parameters (Table 3). The  $20l$  reflections have  $l = 4n$  only, whereas  $11l$  lines have  $l = -(4n \pm 1)$ . The disagreement between experimental and calculated peak positions is different for different  $11l$  reflections. For  $11\bar{3}$ ,  $11\bar{7}$ ,  $11\bar{11}$ , and  $11\bar{15}$ , the disagreement,  $\Delta d(11l)$ , between  $d_{\text{exp}}(11l)$  and  $d_{\text{cal}}(11l)$

significantly increases the background and generates other divergences that do not permit us to accept this model.

**Subcell II.** Figure 6b shows the mutual arrangement of atoms defining the interlayer region when adjacent lay-

**TABLE 2A.** Description of the different models for the position of interlayer Ca in the interlayer region of CaBi subcell I ( $c\text{-cos}\beta = -0.007a$ )

	Model 1		Model 2		Model 3		Model 4		
<b>Mn within layer</b>									
x	0		0		0		0		
y	0		0		0		0		
$\xi$	0		0		0		0		
<b>O within layer</b>									
x	0.33	-0.33	0.33	-0.33	0.33	-0.33	0.33	-0.33	
y	0	0	0	0	0	0	0	0	
$\xi$	1.0	-1.0	1.0	-1.0	1.0	-1.0	1.0	-1.0	
<b>Ca interlayer</b>									
x	0.25		0.67*		0.5		0.5		
y	0.25		0*		0		0.5		
$\xi$	3.52		2.61*		3.52		3.52		
<b>H<sub>2</sub>O</b>									
x	0.67	-0.17	0*	0*	0.17*	0.83*	0*		
y	0	0.5	0*	0*	0.5*	0.5*	0*		
$\xi$	2.80*	4.20*	4.4*	-4.4*	2.52*	4.52*	3.52		
<b>Bond lengths</b>									
Mn-O	1.95		1.95		1.95		1.95		
O-Ca <sub>int</sub>	2.65		2.35		2.65		3.05		
Ca <sub>int</sub> -H <sub>2</sub> O	2.30-2.40		2.45		2.45		2.95		
H <sub>2</sub> O-O <sub>next layer</sub>	2.50-3.20		2.35-2.40		2.30-2.40		3.05		

Note:  $a = 5.150$ ,  $b = 2.848$ ,  $c = 7.040$  Å, and  $\beta = 90.3^\circ$ . Atomic coordinates for Mn, O, Ca (Fig. 6a), and H<sub>2</sub>O are given for these models. The  $x$  and  $y$  coordinates are expressed in fraction of  $a$  and  $b$  parameters, respectively. The bond lengths and  $\xi$  are expressed in angstroms to emphasize the thickness of layer and interlayer octahedra.

\* Indicates coordinates that could be adjusted to obtain reasonable average Ca-O (2.30-2.40 Å) and Ca-H<sub>2</sub>O (2.45-2.55 Å) bond lengths.

reaches 0.006 Å and is systematically beyond experimental error estimated as  $\pm 0.002$  Å [ $\Delta d(11l) = d_{\text{cal}}(11l) - d_{\text{exp}}(11l)$ ]. Moreover,  $\Delta d(11l) > 0$  for all reflections with  $l = -(4n - 1)$ . It was found that  $\Delta d(11l)$  strongly de-

pends on the  $b$  parameter (Table 3). For example,  $\Delta d(11l)$  strongly increases for reflections with  $l = -(4n + 1)$  if  $b = 2.824$  Å, whereas  $\Delta d(11l)$  does not exceed 0.003 Å for reflections with  $l = -(4n - 1)$ . On the contrary, if  $b$

**TABLE 2B.** Description of the different models for the position of interlayer Ca in the interlayer region of CaBi subcell II ( $c\text{-cos}\beta = -0.236a$ )

	Model 1		Model 2		Model 3		Model 4		
<b>Mn within layer</b>									
x	0		0		0		0		
y	0		0		0		0		
$\xi$	0		0		0		0		
<b>O within layer</b>									
x	0.33	-0.33	0.33	-0.33	0.33	-0.33	0.33	-0.33	
y	0	0	0	0	0	0	0	0	
$\xi$	1.0	-1.0	1.0	-1.0	1.0	-1.0	1.0	-1.0	
<b>Ca interlayer</b>									
x	0.40		0.67*		0.40		0.20		
y	0		0		0.5		0.25		
$\xi$	3.52		2.70*		3.52		3.52		
<b>H<sub>2</sub>O</b>									
x	0.05*	0.75*	0.31*	0.11*	0.69	0.89	0.9*	0.55*	-0.15*
y	0.5*	0.5*	0.5	0*	0.5	0	0.5*	0.5*	0.5
$\xi$	3.52*	3.52*	3.52	3.52*	-3.52	-3.52	3.52*	4.8*	2.2
<b>Bond lengths</b>									
Mn-O	1.95		1.95		1.95		1.95		
O-Ca <sub>int</sub>	2.55		2.40		2.90		2.70-2.90		
Ca <sub>int</sub> -H <sub>2</sub> O	2.50		2.40-2.50		2.55		2.20		
H <sub>2</sub> O-O <sub>next layer</sub>	2.50-2.60		2.75-2.90		2.55		2.30		

Note:  $a = 5.150$  Å,  $b = 2.848$  Å,  $c = 7.144$  Å, and  $\beta = 99.8^\circ$ . Atomic coordinates for Mn, O, Ca (Fig. 6b), and H<sub>2</sub>O are given for these models. The  $x$  and  $y$  coordinates are expressed in fraction of  $a$  and  $b$  parameters, respectively. The bond lengths and  $\xi$  are expressed in angstroms to emphasize the thickness of layer and interlayer octahedra.

\* Indicates coordinates that could be adjusted to obtain reasonable average Ca-O (2.30-2.40 Å) and Ca-H<sub>2</sub>O (2.45-2.55 Å) bond lengths.

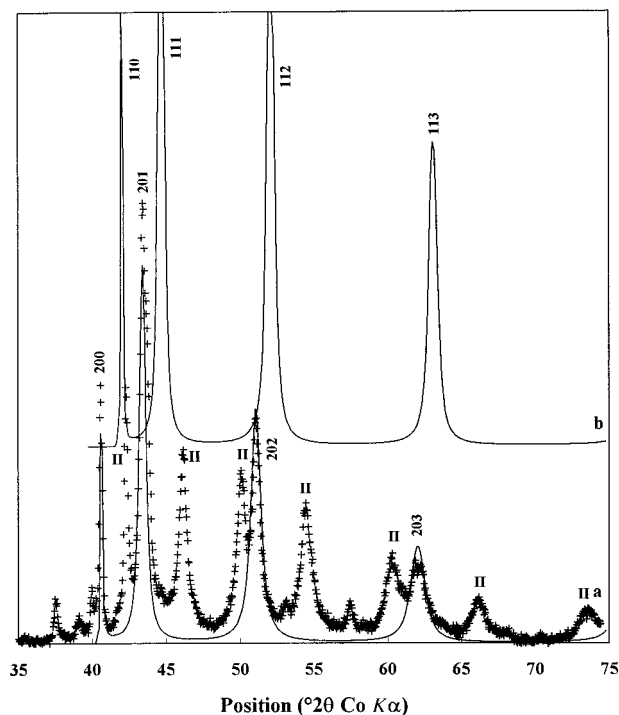


**FIGURE 7.** Comparison between experimental and calculated XRD patterns for model 1, subcell I. Experimental points are shown as crosses, and calculated pattern is plotted as a solid line. Only  $20l$  diffraction lines (a) or only  $11l$  lines (b)  $a = 5.150$ ,  $b = 2.848$ ,  $c = 7.04$  Å, and  $\beta = 90.3^\circ$  are shown. The symbol II indicates experimental diffraction lines of subcell II.

$= 2.848$  Å then  $\Delta d(11l)$  for reflections with  $l = -(4n + 1)$  does not exceed  $0.003$  Å, but  $\Delta d(11l)$  increases for reflections with  $l = -(4n - 1)$ . Finally, in spite of some discrepancies, the four-layer subcell permitted us to index all strong reflections using an intermediate  $2.844$  Å for the  $b$  parameter but failed to account for weak XRD maxima. All these weak maxima corresponded to supercell reflections.

### Indexing of XRD superreflections

As derived from SAED data, all birnessite varieties exhibit an  $A = 3a = 15.45$  Å super-periodicity that did allow us to index most of the superreflections in the experimental XRD pattern (Table 4). All indexed superreflections have  $h0l$  indices, and no super-periodicity along the  $b$  axis was identified in the XRD pattern. Additionally, the  $10.08$  superreflection ( $d_{10.08} = 1.412$  Å) exactly coincides with one of the  $020$  reflections.

### Defect-free structural model for Ca-exchanged birnessite subcell

Two results obtained from the previous analysis of the experimental XRD pattern helped us to find an idealized structure for CaBi: (1) All  $20l$  reflections have  $l = 4n$  in the four-layer subcell and the  $\beta$  angle is similar in both the four-layer subcell and the one-layer subcell I; and (2)

relative intensities of the experimental  $20l$  reflections are very similar to those calculated for model 1 (subcell I). As a consequence, we considered that the structure of CaBi has a one-layer periodicity in a projection along the  $b$  axis and that the atomic arrangement in this projection is similar to model 1 (subcell I). Therefore the increased periodicity along the  $c$  axis may be due to displacements along the  $b$  axis only. The atomic coordinates and site occupancy determined for model 1 (subcell I) (Fig. 6a) are used for layer pairs when there is no such displacement. In the rest of this paper, this stacking of layer pairs without translation along the  $b$  axis is termed O. For adjacent layers shifted, with respect to each other, along the  $b$  axis this shift must be quantified. In particular, a displacement of one layer with respect to the preceding one by  $b/2$  generates an interlayer region very favorable from a crystal chemical point of view and similar to that of Mg-exchanged birnessite (Post and Veblen 1990). All possible positions for Ca cations in such interlayer regions are shown in Figure 8. Models 2 and 3 seem unattractive for the same crystal chemical considerations as for models 3 and 4 (subcell II) (Fig. 6b). In the rest of the paper, only model 1 is considered, because it was the only one that provided positive results. This stacking of layer pairs with a  $b/2$  shift along the  $b$  axis is termed S. There are only two distinct combinations of O and S stackings giving a four-layer structure with the required cell parameters. They are OSOS and OOSS.

Calculations of XRD patterns were limited to the  $40$ – $75^\circ$   $2\theta$   $\text{CoK}\alpha$  region because  $20l$  and  $11l$  reflections are more sensitive to layer stacking and site occupancy than to atomic coordinates, displacement factor, and so forth. Optimum atomic positions, site occupancies, shifts in between adjacent layers, and other calculation parameters are detailed in Table 5 for both O and S stacking vectors. Diffraction patterns calculated for the OOSS model contain strong  $11l$  reflections with  $l = 2n$  that are absent in the experimental XRD pattern; thus, this model was rejected. Figures 9a and 9b compare experimental XRD patterns with the ones calculated for the OSOS model with  $b = 2.824$  Å and  $b = 2.848$  Å, respectively. For both  $b$  values, relative intensities of the experimental and calculated  $11l$  reflections are quite similar, whereas calculated  $20l$  reflections are almost one-half as intense as experimental ones.

The most remarkable result is the position misfit observed for part of the calculated reflections. As can be seen in Figure 9a, for the model with  $b = 2.824$  Å, positions of experimental and calculated  $11l$  reflections with  $l = -(4n - 1)$  and  $20l$  reflections are coincident, whereas  $11l$  reflections with  $l = -(4n + 1)$  are significantly shifted toward higher  $2\theta$  values. On the contrary, for the model with  $b = 2.848$  Å (Fig. 9b) positions of experimental and calculated  $11l$  reflections with  $l = -(4n + 1)$  and  $20l$  reflections agree, whereas  $11l$  reflections with  $l = -(4n - 1)$  are shifted toward lower  $2\theta$  values. This divergence between experimental and calculated positions of  $11l$  reflections was minimized, but not suppressed

**TABLE 3.** Indexing of the experimental XRD pattern of CaBi with a four-layer C-centered monoclinic subcell

Experimental	$b = 2.844 \text{ \AA}$			$b = 2.824 \text{ \AA}$			$b = 2.848 \text{ \AA}$		
	$hkl$	$d_{\text{cal}}(hkl)$	$\Delta d(hkl)$	$hkl$	$d_{\text{cal}}(hkl)$	$\Delta d(11l)$	$hkl$	$d_{\text{cal}}(hkl)$	$\Delta d(11l)$
9.941*									
7.703*									
7.051	004	7.040	-0.011	004	7.040		004	7.040	
5.865*									
5.554*									
3.866*									
3.513	008	3.520	0.007	008	3.520		008	3.520	
3.378*									
3.210*									
2.778*									
2.669*									
2.615*									
2.577	200	2.576	-0.001	200	2.576		200	2.576	
2.477	111	2.480	0.003	111	2.467	-0.010	111	2.483	0.006
2.415	204	2.414	-0.001	204	2.414		204	2.414	
2.400 (s)	113	2.408	0.008	113	2.396	-0.004	113	2.410	0.010
2.280	115	2.279	-0.001	115	2.269	-0.011	115	2.281	0.001
2.114	117	2.119	0.005	117	2.111	-0.003	117	2.121	0.007
2.074	208	2.073	-0.001	208	2.073		208	2.073	
2.000*									
1.955	119	1.951	-0.004	119	1.944	-0.011	119	1.952	-0.003
1.860*									
1.781	11.11	1.787	0.006	11.11	1.782	0.001	11.11	1.788	0.007
1.739	20.12	1.739	0.000	20.12	1.739		20.12	1.739	
1.731	20.12	1.730	-0.001	20.12	1.730		20.12	1.730	
1.639	11.13	1.636	-0.003	11.13	1.632	-0.007	11.13	1.637	-0.002
1.497	11.15	1.501	0.004	11.15	1.498	0.001	11.15	1.501	0.004
1.469	310	1.470	0.001	310	1.470		310	1.470	
1.452	20.16	1.449	-0.003	20.16	1.449		20.16	1.449	
1.424	020	1.422	-0.002	020	1.422		020	1.422	
1.412*									
1.382	11.17	1.381	-0.001	11.17	1.378	-0.004	11.17	1.381	-0.001
1.358	318	1.358	0.000	318	1.356		318	1.359	
1.335									
1.290									
1.270	11.19	1.275	0.005	11.19	1.273	0.003	11.19	1.275	0.005
1.268									

Note:  $a = 5.150 \text{ \AA}$ ,  $c = 4c' = 28.16 \text{ \AA}$ , and  $\beta = 90.3^\circ$ . Calculated  $d_{\text{cal}}(hkl)$  reflection positions are compared to experimental  $d_{\text{cal}}(hkl)$  ones for  $b = 2.844, 2.824$ , and  $2.848 \text{ \AA}$ .  $\Delta d(hkl) = d_{\text{cal}}(hkl) - d_{\text{exp}}(hkl)$ . (s) indicates that the 2.400 Å line is a shoulder difficult to index accurately.

\* Indicates additional lines related to supercells.

**TABLE 4.** Indexing of the superreflections of the experimental XRD pattern of CaBi with a four-layer C-centered monoclinic subcell

Experimental	$b = 2.844 \text{ \AA}$	
	$hkl$	$d_{\text{cal}}(hkl)$
9.941*	buserite?	
7.703*	200	7.728
5.865*		
5.554*		
3.866*	400	3.864
3.378*	404	3.380
3.210*	208	3.210
2.778*		
2.669*		
2.615*	408	2.609
2.000*	40.12	2.001
1.860*	804	1.861
1.412*	10.08	1.412

Note:  $A = 3a = 15.450 \text{ \AA}$ ,  $B = 3b = 8.532 \text{ \AA}$ ,  $c = 4c' = 28.16 \text{ \AA}$ ,  $\alpha = 90^\circ$ , and  $\beta = 90.3^\circ$ .

completely, by using  $b = 2.844 \text{ \AA}$  (Fig. 9c). In addition, a strong discrepancy between calculated and experimental intensities for 20l reflections also shows that the present model can still be improved. We found that it was not possible to obtain a satisfactory fit between experimental and calculated XRD patterns by mixing OSOS models with different  $b$  parameters.

#### Origin of the peak position misfit

Méring (1949) proposed a model to predict the diffraction behavior of basal reflections from structures composed of randomly interstratified layers of different thickness and composition. According to this author, basal reflections for a randomly interstratified mixed-layer structure containing two components are located, in reciprocal space, in between neighboring 00l nodes from both periodic structures each consisting of one interstratified layer type. Positions of basal reflections for the mixed-layer structure vary in between these nodes as a function of the relative proportions of interstratified layers. Usually XRD patterns of randomly interstratified mixed-layer structures differ from those of strictly peri-

**TABLE 5.** Structural parameters used for the simulation of X-ray diffraction profiles

	O		S			
<b>Mn within layer</b>						
<i>x</i>	0		0			
<i>y</i>	0		0			
$\xi$	0		0			
Occ.	1.0		1.0			
<b>O within layer</b>						
<i>x</i>	0.33	-0.33	0.33	-0.33		
<i>y</i>	0	0	0	0		
$\xi$	1.0	-1.0	1.0	-1.0		
Occ.	1.0	1.0	1.0	1.0		
<b>Ca interlayer</b>						
<i>x</i>	0.25	0.25	0.25			
<i>y</i>	0.25	-0.25	0			
$\xi$	3.52	3.52	3.52			
Occ.	0.055	0.055	0.11			
<b>H<sub>2</sub>O interlayer</b>						
<i>x</i>	0.67	-0.17	0.00	0.583	-0.083	0
<i>y</i>	0	0.5	0.67	0.5	0.5	0.25
$\xi$	2.80	4.20	3.52	3.52	3.52	3.52
Occ.	0.40	0.40	0.20	0.30	0.30	0.20
<b>Shift of the next layer</b>						
<i>a</i>	-0.007/ $\sigma$ = 0.06		-0.007/ $\sigma$ = 0.06			
<i>b</i>	0/ $\sigma$ = 0		0.50/ $\sigma$ = 0			
<i>c</i>	7.04/ $\sigma$ = 0		7.04/ $\sigma$ = 0			

Note: All parameters have been adjusted to fit the experimental profiles (Fig. 12).  $a = 5.150$ ,  $b = 2.844$ ,  $c = 4c' = 28.16$  Å, and  $\beta = 90.3^\circ$ . The  $x$  and  $y$  coordinates are expressed in fractions of  $a$  and  $b$  parameters, respectively. The bond lengths and  $\xi$  are expressed in angstroms to emphasize the thickness of layer and interlayer octahedra.

Additional positions within layers are obtained with translation  $(\frac{1}{2}, \frac{1}{2}, 0)$ .

The radius of the CSDs in the  $a$ - $b$  plane is 350 Å. The mean coherent scattering domain ( $N$ ) along the  $c^*$  axis is 16 layers, whereas the maximum  $N$  is 80 layers. No random stacking faults were introduced.

The shift between adjacent layers is expressed in fractions of  $a$  and  $b$  parameters, along the  $a$  and  $b$  axes, respectively, and in angstroms along the  $c$  axis. The symbol  $\sigma$  is the deviation coefficient around the mean value.

odic structures by the presence of a non-rational series of basal reflections. Drits and McCarty (1996) showed that analogous diffraction effects are observed for structures where disorder results from random interstratification of layer fragments that have the same thickness but different internal structures and interlayer displacements. In these cases, the positions of  $hkl$  reflections may be irrational. As in Mering's case study, the non-basal reflections are located in between neighboring  $hkl$  nodes having the same  $hk$  indices and belonging to each of the interstratified minerals. In the light of this work, the non-rational positions of  $11l$  reflections in the experimental XRD pattern may be thought of in terms of random interstratification between two 28.16 Å components having different internal structures and interlayer displacements.

### Defective structural model

Because the positions of  $20l$  reflections are perfectly described by the subcell, we realistically assume that the second 28.16 Å interstratified component differs from the OSOS component by layer displacement along the  $b$  axis. We calculated XRD patterns for triclinic models such as

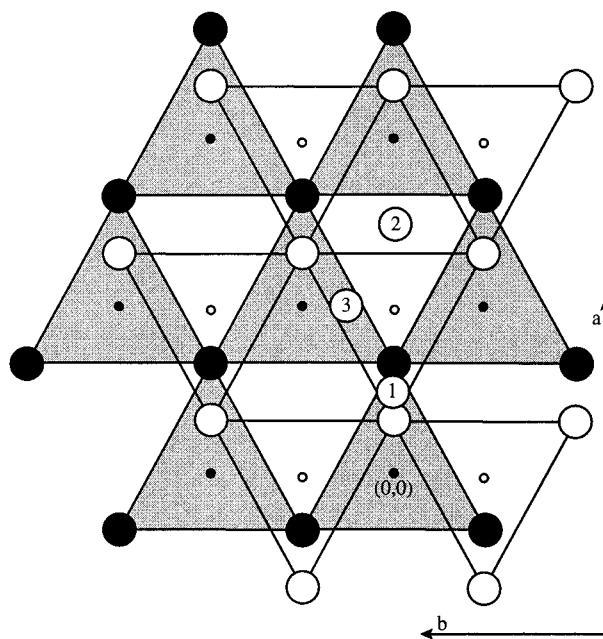


**FIGURE 8.** Possible positions of Ca in the shifted (S) inter-layer space of CaBi S stack. Adjacent layers are translated by  $c \cdot \cos\beta = -0.007a$  and  $b/2$  along the  $a$  and  $b$  axes, respectively. Symbols and notations as in Figure 6a.

OOOS and OSSS. A remarkable feature of the diffraction pattern calculated for the OOOS model (Fig. 10) is that it has almost zero intensity in the vicinity of experimental  $11l$  reflections with  $l = -(4n - 1)$  and has strong diffraction maxima situated not far from experimental  $11l$  reflections with  $l = -(4n + 1)$ . Moreover the latter reflections are always shifted with respect to the calculated ones toward higher  $2\theta$  values. From the above considerations, we can predict the diffraction effects for a CaBi structure in which 28.16 Å OSOS and OOOS components alternate at random. Because the projection of OSOS and OOOS structures coincide along the  $b$  direction of their unit cells, the waves scattered in the direction of the  $20l$  reflections are in phase. Therefore  $20l$  reflections of the interstratified structure are not affected by interstratification effects. A similar effect should occur for  $11l$  reflections with  $l = -(4n - 1)$ , since the waves scattered in the direction of these maxima by the OSOS component should be very slightly affected by the waves scattered by the OOOS component because of their extremely weak amplitudes. On the contrary, the  $11\bar{1}$ ,  $11\bar{5}$ ,  $11\bar{9}$ , and  $11.1\bar{3}$  reflections of the OSOS model should migrate respectively toward  $110$ ,  $114$ ,  $118$ , and  $11.12$  reflections of the OOOS model with increasing proportion of the OOOS component in the interstratified structure. In other words, these reflections should migrate toward neighboring experimental ones. Figure 11 compares the experimental XRD pattern with that calculated for the interstratified structural model consisting of the OSOS (90%) and OOOS (10%) components. Both components have  $b =$

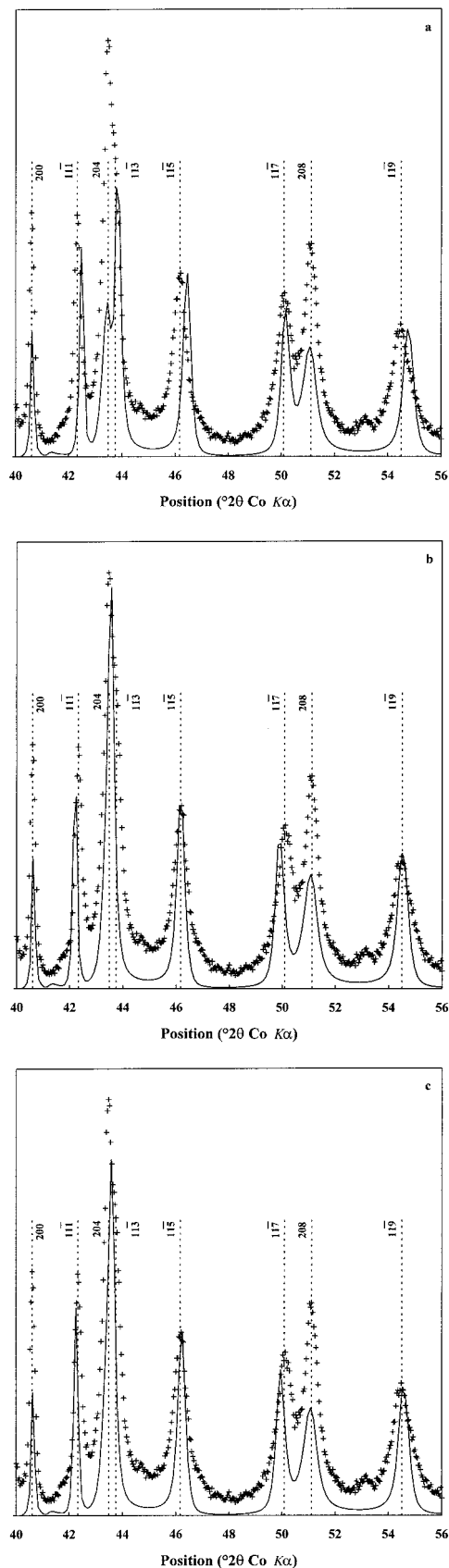


**FIGURE 9.** Comparison between experimental and calculated XRD patterns for the OSOS model. OSOS models were calculated for  $b = 2.824 \text{ \AA}$  (a),  $b = 2.848 \text{ \AA}$  (b), and  $b = 2.844 \text{ \AA}$  (c). Patterns as in Figure 7.

←

$2.844 \text{ \AA}$ . As can be seen in Figure 11, the general agreement between calculated and experimental positions and intensity distributions is much better than for the OSOS periodic structure with the same  $b$  value (Fig. 9c). However some discrepancy is still observed for the  $11\bar{1}$ ,  $11\bar{7}$ , and  $11.\bar{1}\bar{1}$  reflections.

#### Actual crystal structure

As mentioned in the beginning of the Results section, the experimental diffraction pattern contains two 020 reflections, one of which with  $d = 1.412 \text{ \AA}$  overlaps with the sharp 10.08 superreflection whereas the other one is broadened and its exact position cannot be measured with a high precision ( $d \approx 1.424 \text{ \AA}$ ). We assumed that this broadened maximum corresponds to the interstratified structure described above and that the 020 reflection with  $d = 1.412 \text{ \AA}$  corresponds to the defect-free OSOS variety with  $b = 2.824 \text{ \AA}$ . Figure 12 shows the best agreement that was obtained for a physical mixture of the defect-free OSOS variety with  $b = 2.824 \text{ \AA}$  and the defective interstratified phase consisting of interstratified OSOS and OOS components (9:1) with  $b = 2.844 \text{ \AA}$ .

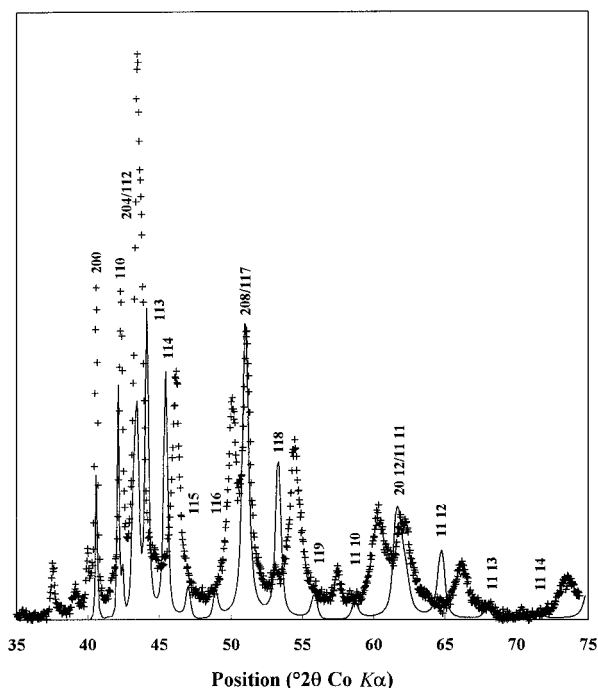


**FIGURE 10.** Comparison between experimental and calculated XRD patterns for the OOS model with  $b = 2.844 \text{ \AA}$ . Patterns as in Figure 7. For this model  $11\bar{1}$  and  $11\bar{7} + \bar{1}$  lines are superimposed.

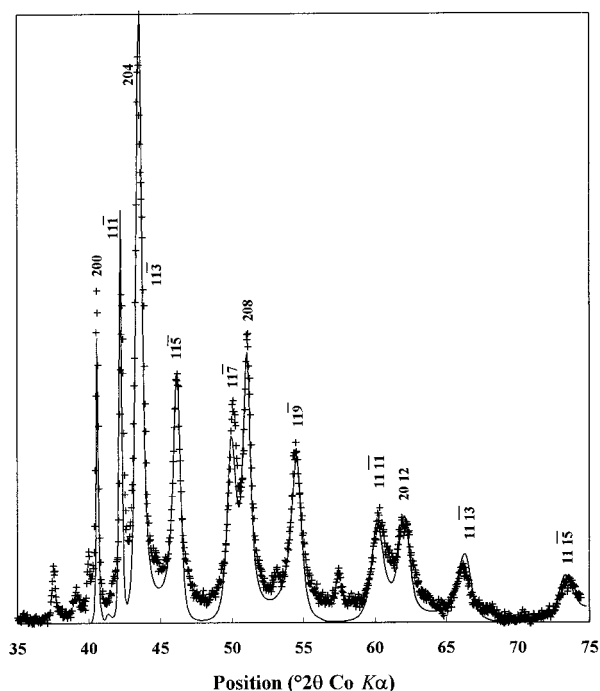


**FIGURE 11.** Comparison between experimental and calculated XRD patterns for the interstratified OSOS-OOOS structural model. This model contains 90% of the OSOS component and 10% of the OOOS one and is randomly interstratified. Both components have  $b = 2.844 \text{ \AA}$ . Patterns as in Figure 7.

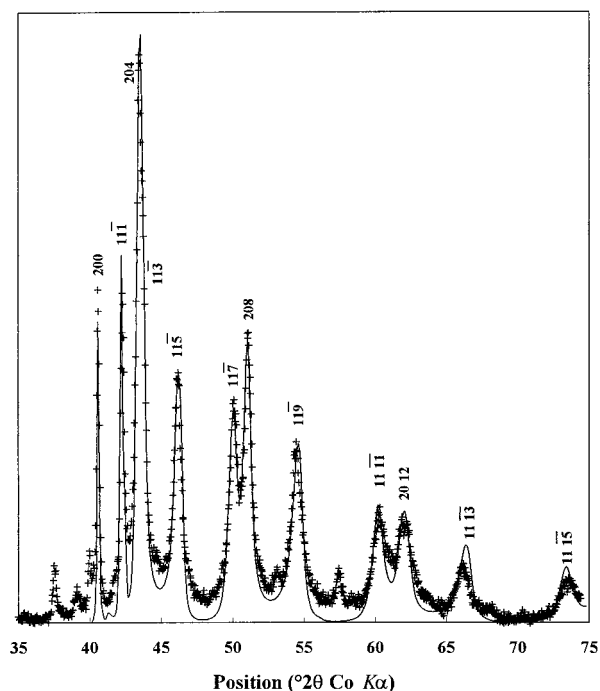


**FIGURE 12.** Comparison between experimental and calculated XRD patterns. The calculated pattern is the sum of the interstratified structural model shown in Figure 9 (90% OSOS, 10% OOOS, random interstratification,  $b = 2.844 \text{ \AA}$  for both components) and of the defect-free OSOS variety ( $b = 2.824 \text{ \AA}$ ). Patterns as in Figure 7.

### Superstructures

Comparison of the present data with the results obtained by Drits et al. (1997) and Silvester et al. (1997) shows that CaBi and NaBi have several common features. (1) The superreflections in SAED patterns of these compounds originate from an ordered distribution of interlayer cations and  $\text{H}_2\text{O}$  molecules because the great variety of SAED effects observed for NaBi and CaBi crystals having similar layer structures and cation compositions cannot be explained only by different vacancy distributions as suggested in previous studies. It is more reasonable to assume that the different interlayer structures reflect contrasting total layer charge and layer-charge distribution. (2) The main source of negative layer charge is the presence of layer  $\text{Mn}^{3+}$ . Indirect evidence for this hypothesis results from the  $a/b$  ratio, which deviates from  $\sqrt{3}$  in CaBi as in all cation-exchanged monoclinic birnessite samples because of the presence of distorted  $\text{Mn}^{3+}$  octahedra (Jahn-Teller effect) with their long Mn-O distances preferentially oriented along the  $a$  axis. (3) In both NaBi and CaBi structures  $\text{Mn}^{4+}$  and  $\text{Mn}^{3+}$  cations have ordered distributions.  $\text{Mn}^{3+}$  octahedra are elongated along the  $a$  axis and share edges to form chains parallel to the  $b$  axis. These  $\text{Mn}^{3+}$ -rich rows alternate regularly along the  $a$  axis with two  $\text{Mn}^{4+}$ -rows forming an  $\text{Mn}^{3+}\text{Mn}^{4+}\text{Mn}^{4+}$  sequence, this regular alternation inducing the  $A = 3a$  super-periodicity in NaBi and CaBi. This

super-periodicity was described by Kuma et al. (1994) in most cation-exchanged monoclinic birnessite samples. These data may be considered as evidence for a recurrent ordered distribution of heterovalent layer Mn cations in most birnessite formed at high pH. As a consequence of these  $\text{Mn}^{3+}$ -rich rows, undersaturated O atoms are linearly arranged in rows parallel to the  $b$  axis, with the actual undersaturation of these O atoms dependant on the possible presence of  $\text{Mn}^{4+}$  and vacancies in these rows. The maximum undersaturation of the O atoms appears when  $\text{Mn}^{3+}$ -rich rows contain vacant octahedra.

$\text{Mn}^{3+}$ -rich rows of adjacent layers are supposed to be close to each other in CaBi as in NaBi, even though their relative positions are not strictly identical as demonstrated by their different  $\beta$  angles ( $90.3^\circ$  and  $103.2^\circ$ , respectively). In the CaBi structure, nearest  $\text{Mn}^{3+}$  and  $\text{Mn}^{4+}$  rows of one layer coincide in projection on the  $a$ - $b$  plane with  $\text{Mn}^{4+}$  and  $\text{Mn}^{3+}$  rows of the adjacent layer, respectively (Fig. 13). Such arrangement of the  $\text{Mn}^{3+}$ -rich rows leads to the formation of pairs of strongly undersaturated O atoms. These pairs of undersaturated O atoms are linearly arranged along the  $b$  axis and alternate along the  $a$  axis with a periodicity equal to  $A = 3a$ . Because these O pairs create periodically distributed linear regions with a high negative charge in the interlayer space, Ca cations should also be linearly arranged along the  $b$  axis to provide local charge compensation to pairs of strongly undersaturated



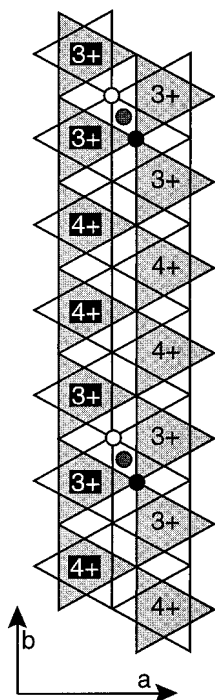


**FIGURE 13.** Schematic representation of the relative positions of  $\text{Mn}^{3+}$ -rich rows in two adjacent layers. Adjacent layers are displaced, with respect to each other, by  $c \cdot \cos\beta = -0.007a$  along the  $a$  axis. The upper surface of the lower layer and the lower surface of the upper layer are shown respectively as shaded and unshaded triangles as in Figure 6a.  $\text{Mn}^{3+}$  and  $\text{Mn}^{4+}$  in  $\text{Mn}^{3+}$ -rich rows are shown as 3+, 4+;  $\text{Mn}^{4+}$  rows are not shown. Black labels indicate the valency of Mn cations belonging to the lower layer, whereas white labels in black squares indicate the valency of Mn cations belonging to the upper layer. Only the most undersaturated O atoms from the lower (solid circles) and from the upper (open circles) layers are shown. The shaded circle represents the position of interlayer Ca.

O atoms (Fig. 13). As a consequence, Ca cations are also distributed with the same  $A = 3a$  super-periodicity.

**Superstructure of CaBi type I ( $A = 3a$ ,  $B = 3b$ ,  $\gamma = 90^\circ$ ).** The interlayer space for the first layer pair of the OSOS superstructure is represented in Figure 14a. Ca cations have a local environment found for model 1 (subcell I) that is, they are coordinated by two O atoms belonging to adjacent layers and the four  $\text{H}_2\text{O}$  molecules. The positions of  $\text{H}_2\text{O}$  molecules also correspond to those found for model 1 (subcell I) Ca cations and  $\text{H}_2\text{O}$  are distributed

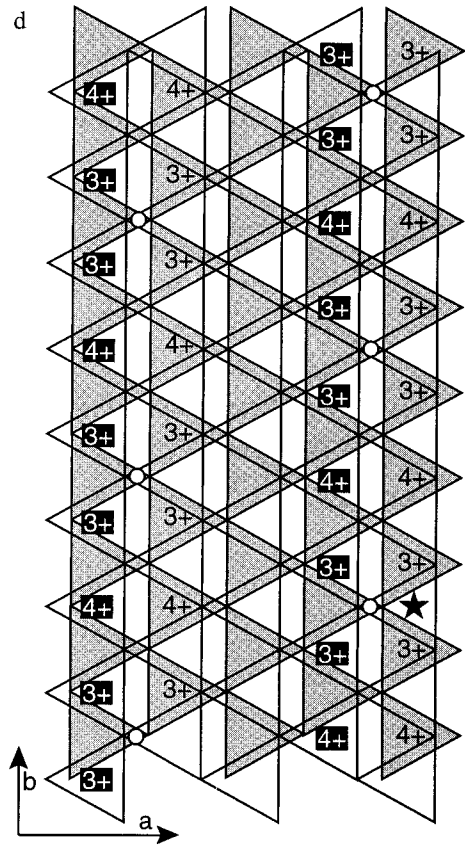
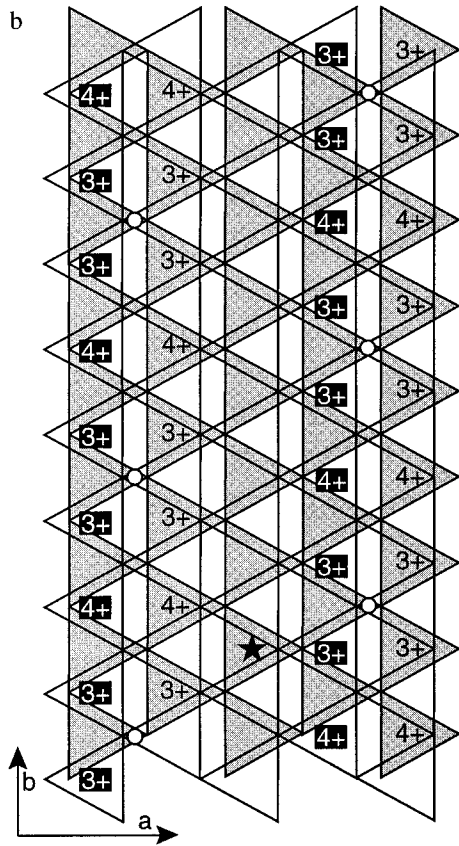
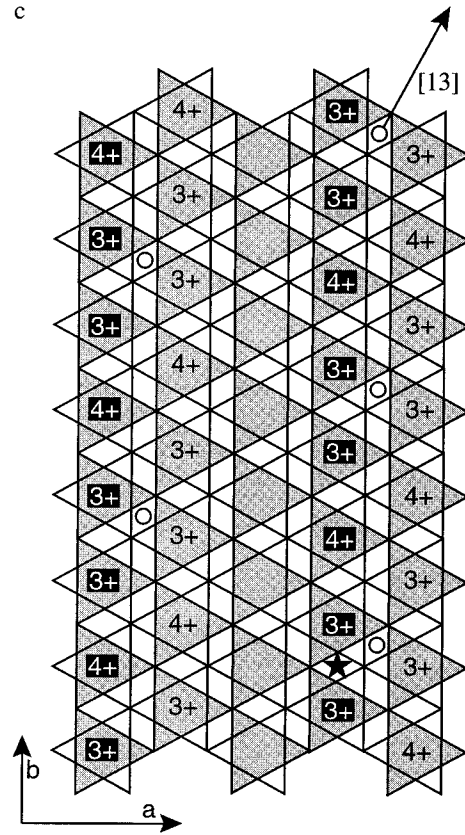
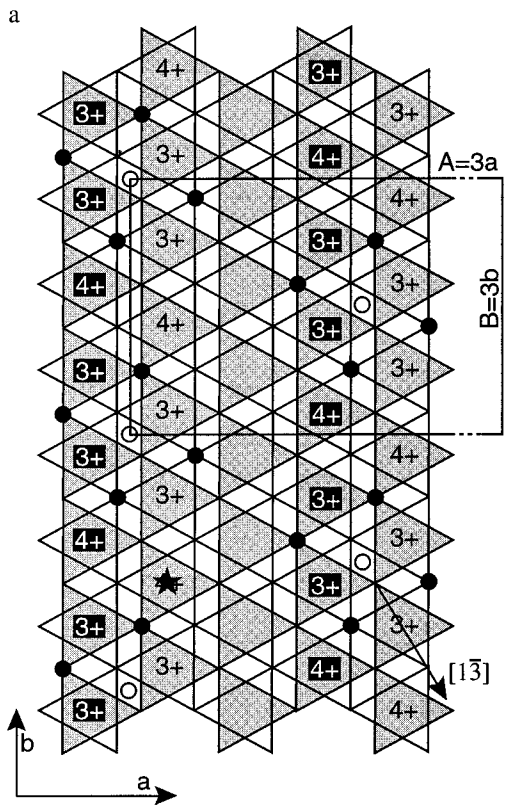
to form the  $C$ -centered supercell with  $A = 3a$  and  $B = 3b$ . There are only two sites, with coordinates 0,0 and 0.5,0.5, available for hydrated Ca cations within the supercell. If the interlayer space of this CaBi variety contains only Ca cations, then the total negative layer charge of the supercell is  $-4$  v.u., compensated by two  $\text{Ca}^{2+}$ . Since the supercell contains 18 octahedral sites, the chemical composition of this CaBi variety can be expressed as  $\text{Ca}_2(\text{Mn}_4^{3+}\text{Mn}_{14}^{4+})\text{O}_{36}$ . Taking into account the ordered distribution of  $\text{Mn}^{4+}$ - and  $\text{Mn}^{3+}$ -rich rows along the  $a$  axis, the  $\text{Mn}^{3+}:\text{Mn}^{4+}$  ratio in  $\text{Mn}^{3+}$ -rich rows should be 2:1, and heterovalent Mn in  $\text{Mn}^{3+}$ -rich rows is likely to be distributed according to the  $\text{Mn}^{4+}\text{Mn}^{3+}\text{Mn}^{3+}$  sequence. If  $\text{Mn}^{4+}\text{Mn}^{3+}\text{Mn}^{3+}$  sequences in two adjacent layers are shifted by  $(\mathbf{b} - \mathbf{a})/2$  (Figs. 13 and 14a), then most undersaturated O atoms belonging to adjacent layers are closely located and form pairs aligned along  $[1\bar{3}]$  in projection on the  $a$ - $b$  plane (Fig. 14a). These pairs are automatically distributed along the  $a$  and  $b$  axes with the  $A = 3a$  and  $B = 3b$  periodicity of the supercell. Ca cations are located in the centers of these pairs to provide a local charge compensation. The proposed arrangement of  $\text{Mn}^{3+}$ -rich rows in adjacent layers, together with the ordered distribution of heterovalent Mn in these rows, explains why Ca is coordinated by only two O atoms belonging to different layers, these O atoms being the most undersaturated ones (Fig. 13).

The second interlayer space of the OSOS superstructure is characterized by the  $b/2$  shift, along the  $b$  axis, between adjacent layers (S stack). As a result, Mn cations of neighboring  $\text{Mn}^{3+}$ -rich rows of these adjacent layers are facing each other in projection on the  $a$ - $b$  plane (Fig. 14b). The  $\text{Mn}^{4+}\text{Mn}^{3+}\text{Mn}^{3+}$  sequence of the third layer is shifted by  $-\mathbf{a}/2$  with respect to the same sequence of the second layer. In this second interlayer (S stack), pairs of most undersaturated O atoms are aligned along the  $a$  axis and are distributed with  $A = 3a$  and  $B = 3b$ . Ca cations are coordinated by these O pairs providing local layer charge compensation as in the first interlayer (O stack).

To provide identical cation arrangements in the first and fifth layers of the OSOS superstructure, the  $\text{Mn}^{4+}\text{Mn}^{3+}\text{Mn}^{3+}$  sequence of the fourth layer must be shifted with respect to the same sequence of the third layer by  $-(\mathbf{a} + \mathbf{b})/2$  (Fig. 14c; third interlayer, O stack). In this case, the pairs of the most undersaturated O atoms are oriented along  $[1\bar{3}]$  in projection on the  $a$ - $b$  plane. Ca cations coordinated by these O atoms are again distributed periodically with  $A = 3a$ ,  $B = 3b$ , and  $\gamma = 90^\circ$ . The

→

**FIGURE 14.** Model showing the displacements between adjacent layers and the distribution of Ca and  $\text{H}_2\text{O}$  molecules in the interlayer regions of CaBi type I. In this variety, heterovalent Mn atoms are distributed according to the  $\text{Mn}^{4+}\text{Mn}^{3+}\text{Mn}^{3+}$  sequence in  $\text{Mn}^{3+}$ -rich rows. **a**, **b**, **c**, and **d** refer respectively to the first, second, third, and fourth interlayer regions of the OSOS stack. Patterns as in Figure 13, except for solid and open circles, which correspond to interlayer Ca and  $\text{H}_2\text{O}$ , respectively. O atoms from the layers are not shown. In Figure 14b and 14d,  $\text{H}_2\text{O}$  molecules are located exactly above or below  $\text{Mn}^{3+}$  and are not shown. Local environments of Ca in the third and fourth interlayers are similar to those in the first and second interlayers, respectively. The solid star indicates the origin in the first layer and is shown subsequently to indicate the total shift from that first layer.





fourth interlayer region (Fig. 14d; S stack) is identical to the second one, the  $\text{Mn}^{4+}\text{Mn}^{3+}\text{Mn}^{3+}$  sequence of the fifth layer being shifted with respect to the same sequence of the fourth layer by  $-\mathbf{a}/2$ . Additionally, a glide plane connects successive odd layers as well as successive even layers.

**Superstructure of CaBi type II.** The interlayer space for the first layer pair of the OSOS superstructure is shown in Figure 15a. Ca cations are coordinated by two O atoms belonging to adjacent layers and four  $\text{H}_2\text{O}$  molecules. Ca and  $\text{H}_2\text{O}$  are distributed to form a primitive unit cell with  $A_p = \frac{3}{2}(\mathbf{a} + \mathbf{b})$ ,  $B_p = -4\mathbf{b}$  in this first interlayer. As for CaBi type I, there are no additional sites for hydrated Ca cations in this supercell. If Ca is the only interlayer cation then the total negative charge of the supercell is  $-2$  v.u., compensated by one  $\text{Ca}^{2+}$ . Because the supercell contains 12 octahedral layer sites, the chemical composition of CaBi type II is  $\text{Ca}(\text{Mn}_3^{3+}\text{Mn}_{10}^{4+})\text{O}_{24}$ , which implies that the  $\text{Mn}^{3+}:\text{Mn}^{4+}$  ratio in  $\text{Mn}^{3+}$ -rich rows is 1:1. In these rows, a regular  $\text{Mn}^{3+}\text{Mn}^{3+}\text{Mn}^{4+}\text{Mn}^{4+}$  distribution of heterovalent Mn automatically leads to the distribution of most undersaturated O pairs with the periodicity of the superlattice (Fig. 15a). These O atoms form pairs if the  $\text{Mn}^{3+}\text{Mn}^{3+}\text{Mn}^{4+}\text{Mn}^{4+}$  sequence of the second layer is shifted with respect to the same sequence of the first layer by  $(\mathbf{b} - \mathbf{a})/2$ . Ca cations are coordinated by these O pairs to provide a local layer charge compensation and are also distributed with the periodicity of the superlattice. Additionally, Figure 15a shows that interlayer Ca atoms are oriented along  $[\bar{1}\bar{3}]$  in the projection on the  $a$ - $b$  plane.

The relative positions of  $\text{Mn}^{3+}\text{Mn}^{3+}\text{Mn}^{4+}\text{Mn}^{4+}$  sequences and of interlayer Ca in successive layers of the OSOS superstructure are shown in Figures 15b, 15c, and 15d. In the second, third, and fourth interlayer regions of this OSOS superstructure, the  $\text{Mn}^{3+}\text{Mn}^{3+}\text{Mn}^{4+}\text{Mn}^{4+}$  sequence of the upper layer is shifted by  $-\mathbf{a}/2$ ,  $-(\mathbf{a} + \mathbf{b})/2$ , and  $-\mathbf{a}/2$ , respectively, with respect to the same sequence of the lower layer (Figs. 15b, 15c, and 15d). In the four interlayer regions, Ca cations are coordinated by pairs of the most undersaturated O atoms. In the second and fourth interlayers, the pairs of most undersaturated O atoms are oriented along the  $a$  axis. In the third interlayer these pairs are oriented along  $[13]$ , which is connected by a glide plane with the first interlayer. Moreover, the primitive unit cell describing the distribution of Ca and  $\text{H}_2\text{O}$  in the second and third interlayers has parameters  $A_p = \frac{3}{2}(\mathbf{a} - \mathbf{b})$ ,  $B_p = +4\mathbf{b}$ ,  $\gamma = 118.9^\circ$ , whereas this primitive unit cell has parameters  $A_p = \frac{3}{2}(\mathbf{a} + \mathbf{b})$ ,  $B_p =$

$-4\mathbf{b}$ ,  $\gamma = 118.9^\circ$  in the first and fourth interlayers. In projection on the  $a$ - $b$  plane, these two primitive cells are connected by a mirror plane. A glide plane connects the first and third layers as well as the second and fourth layers.

## DISCUSSION

These results show that our CaBi sample is characterized by a set of unusual and complex diffraction effects. Quantitative analysis of XRD and SAED patterns showed that this CaBi consists of two main varieties, with the main structural and crystal chemical features determined reliably. The good agreement observed between experimental and calculated intensity distributions vouches for the realism of the proposed model. However the coexistence of two complex CaBi structures, as well as the presence of structural defects, prevents us from assessing atomic positions, site occupancy, and bond lengths in interlayer spaces of these varieties with a high degree of accuracy. In the following section, the origin of the different features characterizing the proposed model is discussed in the light of crystal chemical considerations.

### Origin of the $b/2$ shift between adjacent layers of the S stack

CaBi type I and type II have quite similar substructures, described by the OSOS stacking sequence. Regular displacements of layer pairs by  $b/2$  along the  $b$  axis are probably connected with a tendency to decrease electrostatic repulsion. If all layers in the structure were stacked according to an OOOO sequence, then Mn cations belonging to different layers would all be aligned parallel to  $c^*$ . As a result, electrostatic interaction between layers would be very strong. As can be seen in Figure 8, displacement of one layer with respect to the preceding one by  $b/2$  provides a much more homogeneous distribution of Mn cations in this layer pair, increases the distance between Mn of adjacent layers, and decreases their interactions. Such a mutual arrangement of layers in the structure also favors local charge compensation of the most undersaturated O atoms by  $\text{Ca}^{2+}$  cations. One of the main differences between the two varieties is their different degrees of structural perfection. CaBi type I represents the defect-free structure, whereas CaBi type II contains OOS sequences. This difference is likely to be induced by different layer charges and, as a consequence, by a difference of bond strength between adjacent layers of the two types of CaBi. Because the content of  $\text{Mn}^{3+}$  in CaBi type I prevails over that in CaBi type II by 33% the pro-

←

**FIGURE 15.** Model showing the displacements between adjacent layers and the distribution of Ca and  $\text{H}_2\text{O}$  molecules in the interlayer regions of CaBi type II. In this variety, heterovalent Mn atoms are distributed according to the  $\text{Mn}^{4+}\text{Mn}^{4+}\text{Mn}^{3+}\text{Mn}^{3+}$  sequence in  $\text{Mn}^{3+}$ -rich rows. **a**, **b**, **c**, and **d** refer respectively to the first, second, third, and fourth interlayer regions of the OSOS stack. All patterns as in Figure 14. The primitive unit cells are outlined with dashed lines. In Figure 15b and 15d  $\text{H}_2\text{O}$  molecules are located exactly above or below  $\text{Mn}^{3+}$  and are not shown. Local environments of Ca in the third and fourth interlayers are similar to those in the first and second interlayers, respectively.

portion of Ca is higher in CaBi type I. We note that the smaller supercell dimensions for CaBi type I are correlated with the greater amount of interlayer Ca in this structure.

#### Origin of OOOS defects in Ca-exchanged birnessite type II

The weaker layer bonding in CaBi type II is probably responsible for the presence of defects in the structure. As in both O and S interlayers Ca cations provide local charge compensation, the regular alternation of O and S interlayers may be perturbed only by an additional displacement of adjacent layers by  $b/2$  along the  $b$  axis leading to the formation of S and O interlayers, respectively. These perturbations seem to occur only in S interlayers leading to the alternation of OSOS and OOOS structural fragments. As a consequence of this interstratification the structure cannot be described by a unique lattice because of the non-rationality of  $11l$  reflections. The origin of this effect was described by Drits and McCarty (1996) and was taken into account in this work. From the indexing of XRD patterns of synthetic busierite and birnessite with different exchangeable cations, Kuma et al. (1994; Tables 3e, 3f, 4a, 4b, 4c) has shown that only part of the measured and calculated  $d(hkl)$  values coincide within experimental error. Consequently this interstratification effect may be common to many types of birnessite. It should be emphasized that the present approach consisting of the simulation of diffraction effects from reasonable structural models containing various defects is the most efficient way to reveal the actual crystal structure of such birnessite.

#### Origin of the super-periodicities

Our results are consistent with a model of local sources of negative charge ( $Mn^{3+}$ , vacancies) linearly arranged along the  $b$  axis of synthetic birnessite formed at high pH. According to Kuma et al. (1994) these sources are represented by empty octahedra, whereas Drits et al. (1997) and Silvester et al. (1997) showed that they are represented mainly by  $Mn^{3+}$ . Our calculations showed that CaBi layers do not contain a significant amount of vacancies. As a consequence,  $Mn^{3+}$  and interlayer Ca are also linearly arranged along the  $b$  axis (Figs. 14 and 15). The ordered distribution of  $Mn^{3+}$ -rich and Ca-rich rows along the  $a$  axis with a periodicity of  $A = 3a/2$  is responsible for the appearance of the superreflections in SAED and XRD patterns. Other superreflections are related to the relative proportions and to the ordered distribution of  $Mn^{3+}$  and  $Mn^{4+}$  cations within  $Mn^{3+}$ -rich rows and, as a consequence, to the amount and distribution of interlayer Ca cations along the  $b$  axis.

It is remarkable that all XRD superreflections indexed have only  $h0l$  indices. The absence of superreflections with  $k \neq 0$  may be related to the presence of stacking faults in CaBi type II. In projection along the  $b$  axis, both CaBi varieties have a common defect-free two-dimensional periodicity ( $A = 1.5a$ ,  $C = 4c'$ ). Because of this

common periodicity, the superreflections indexed in the  $A = 3a$ ,  $C = 4c'$  cell (Table 4) have  $h = 2n$ , and  $l = 4n$  and a sharp profile. Such sharp reflections support the hypothesis of an identical  $a$  parameter for both varieties because even slightly different  $a$  parameters would lead to a noticeable broadening of these reflections.

#### Relative positions of $Mn^{3+}$ -rich rows in adjacent layers and local environment of Ca

Drits et al. (1997) have shown that  $Mn^{3+}$ -rich rows in NaBi may contain heterovalent Mn cations, or  $Mn^{4+}$  and vacancies, distributed periodically with  $B = 6b$ . According to the present study, both Ca-exchanged varieties consist essentially of vacancy-free layers in which heterovalent Mn cations are regularly distributed in  $Mn^{3+}$ -rich rows. It is likely that most, if not all, birnessite varieties synthesized at high pH contain  $Mn^{3+}$ -rich rows periodically distributed along the  $a$  axis, whereas the mutual arrangement of  $Mn^{3+}$ -rich rows in adjacent layers seems controlled by the nature of interlayer cations. In other words, the nature of the exchangeable cation determines the layer stack.

Despite the difference of layer charge, Ca cations have almost identical environments in CaBi type I and II. As seen in Figures 14 and 15, each Ca is coordinated to the two most undersaturated O atoms, which are coordinated to two  $Mn^{3+}$  and one  $Mn^{4+}$ . Hydrogen bonds formed by interaction with  $H_2O$  molecules compensate the deficit of charge of other undersaturated O atoms coordinated to one  $Mn^{3+}$  and two  $Mn^{4+}$ .

#### Origin of layer charge variability

Superstructure models for CaBi varieties are idealized. According to chemical analysis, NaBu layer charge is equal to 0.30 v.u. per octahedron, whereas the layer charge determined for CaBi type I is 0.22 v.u. A possible explanation for this discrepancy is the partial oxidation of  $Mn^{3+}$  in  $Mn^{3+}$ -rich row, during or after the cation exchange. On the other hand, it is possible that the actual layer charge, at least in CaBi type I, is higher than what was determined from structural considerations because of only partial substitution of Ca for Na during the cation exchange reaction. This limited cation exchange reaction may be related to the limited number of crystallographic positions in which a divalent cation may provide local charge compensation. In this case, we assume that in  $Mn^{3+}$ -rich rows a small proportion of cations are replaced by vacancies in  $Mn^{4+}Mn^{3+}Mn^{3+}$  cation sequences, the additional negative layer charge being compensated by non-exchangeable Na cations. However little Na was detected from the chemical analysis, and it is unfortunately not possible to determine the presence of Na from the XRD analysis because of its small amount and low scattering power. Even if some Na remained in the interlayers, the main trend in the ordered distribution of heterovalent cations in  $Mn^{3+}$ -rich rows of CaBi type I remains identical. Finally, the total negative charge determined for CaBi type II (0.167 v.u. per octahedron) determined in the pres-

ent study precisely coincides with the layer charge found by Drits et al. (1997) for NaBi type I.

### Origin of *b* parameter variation

The sharp superreflections observed in experimental XRD patterns of CaBi indirectly support the hypothesis of an identical periodicity for both CaBi type I and II along the *a* axis. Additionally, the *a* parameters found for CaBi and Ca-exchanged birnessite, hereafter referred to as CaBu, have the same values (Kuma et al. 1994). However, the XRD pattern of CaBu contains two reflections with *d* values equal to 1.421 and 1.414 Å that are very close to those observed for our CaBi sample (1.424 and 1.412 Å) and that may be attributed to 020 reflections. It means that type I and type II varieties formed at the CaBu stage, that is before dehydration. In the XRD pattern of CaBi (Fig. 1) these two reflections have different profiles, the *d* = 1.412 Å peak is sharp despite its overlap with the 10.08 superreflection, whereas the *d* = 1.424 Å peak is broad. The analysis of SAED patterns showed that *b* = 2.824 Å corresponds to CaBi type I, whereas CaBi type II has a variable parameter *b* = 2.840–2.848 Å.

In the light of previous results (Drits et al. 1997) these results are consistent with the relative proportions of Mn<sup>3+</sup> in both structures. These authors showed that the deviation from the hexagonal symmetry of NaBi is due to the Jahn-Teller distortion of Mn<sup>3+</sup> octahedra: The greater the *a/b* ratio, the greater the amount of Mn<sup>3+</sup> octahedra. Because *a/b* ratios are equal to 1.835 and 1.806 for CaBi type I and II, respectively, CaBi type I should contain a higher amount of Mn<sup>3+</sup> in comparison with CaBi type II. This consideration is in agreement with the chemical composition of CaBi varieties obtained from the structural data.

### Origin of the heterogeneity of Ca-exchanged birnessite crystallites

A distinctive feature of birnessite, regardless of the nature of the exchangeable cation, is the structural heterogeneity. The main factors that control the diversity of birnessite varieties are the density of negative layer charge, the distribution of heterovalent Mn cations in layers, and the nature of the interlayer cation. For these reasons birnessite samples containing the same exchangeable cation may include several varieties with different superstructures (Chukhrov et al. 1979, 1989; Drits et al. 1997). The structural heterogeneity of CaBi crystallites is characterized by the intergrowth of CaBi type I and II and the twinning of CaBi type II. Intergrown crystals have *b* parameters intermediate between 2.824 and 2.848 Å. Because CaBi type I and II have slightly different *b* parameters we can conclude that these intergrown crystals accommodate two-dimensional layer dimensions. Because of this accommodation, their SAED patterns consist of two commensurable reflection networks, with a unique *b* value for both components, instead of two incommensurable ones. Thus, intergrowth may be the reason for the broadening of the 020 reflection as relative intensities of

CaBi type I and II superreflections vary from one crystal to the other. On the contrary, there is no lattice accommodation for twins consisting of CaBi type II sub-crystals that are rotated around *c*\* by 120° (Fig. 5b). As *a/b* ≠ √3, such rotated layers form incommensurable layer lattices.

### ACKNOWLEDGMENTS

The authors thank Ewen Silvester for supplying the synthetic Ca-exchanged birnessite sample and Jeffrey Walker for corrections on an early version of the manuscript. We are also grateful to R. Giovanoli and to A.G. Christy for their constructive reviews of this manuscript and to S. Redfern for his editorial assistance. V.D. acknowledges financial support from the Centre National de la Recherche Scientifique (France). V.D. and A.G. acknowledge financial support from the Russian Foundation for Fundamental Research.

### REFERENCES CITED

- Balistreri, L.S. and Murray, J.W. (1982) The chemistry of δ-MnO<sub>2</sub>. *Geochimica et Cosmochimica Acta*, 46, 1041–1052.
- Bricker, O. (1965) Some stability relations in the system Mn-O<sub>2</sub>-H<sub>2</sub>O at 25° and one atmosphere total pressure. *American Mineralogist*, 50, 1296–1354.
- Burns, R.G. and Burns, V.M. (1977) The mineralogy and crystal chemistry of deep-sea manganese nodules, a polymetallic resource of the twenty-first century. *Philosophical Transactions of the Royal Society of London (A)*, 286, 283–301.
- Burns, V.M. and Burns, R.G. (1978) Post-depositional metal enrichment processes inside manganese nodules from the north equatorial Pacific. *Earth and Planetary Science Letters*, 39, 341–348.
- Buser, W. and Graf, P. (1955) Radiochemische Untersuchungen an Festkörpern III: Ionen- und Isotopenaustauschreaktionen an Mangandioxyden und Manganiten. *Helvetica Chimica Acta*, 38, 811–829.
- Chukhrov, F.V. and Gorshkov, A.I. (1981) Iron and manganese oxide minerals in soils. *Transactions of the Royal Society of Edinburgh*, 72, 195–200.
- Chukhrov, F.V., Gorshkov, A.I., Rudnitskaya, E.S., and Sivtsov, A.V. (1978) Birnessite characterization. *Investiya Akademii Nauk, SSSR, Seriya Geologicheskaya*, 9, 67–76.
- Chukhrov, F.V., Gorshkov, A.I., Sivtsov, A.V., and Beresovskaya, V.V. (1979) New mineral phases of oceanic manganese micro-concretions. *Izvestiya Akademii Nauk SSSR, Seriya Geologicheskaya*, 1, 83–90 (in Russian).
- Chukhrov, F.V., Sakharov, B.A., Gorshkov, A.I., Drits, V.A., and Dikov, Y.P. (1985) Crystal structure of birnessite from the Pacific Ocean. *International Geology Review*, 27, 1082–1088 (translated from *Investiya Akademii Nauk, SSSR, Seriya Geologicheskaya*, 8, 66–73).
- Chukhrov, F.V., Gorshkov, A.I., Berezovskaya, V.V., and Sivtsov, A.V. (1987) New data about mineralogy of Kertch ore deposits. *Izvestiya Akademii Nauk, SSSR, Seriya Geologicheskaya*, 4, 60–77.
- Chukhrov, F.V., Gorshkov, A.I., and Drits, V.A. (1989) Supergenic manganese hydrous oxides, 208 p. Nauka, Moscow.
- Cornell, R.M. and Giovanoli, R. (1988) Transformation of hausmannite into birnessite in alkaline media. *Clays and Clay Minerals*, 36, 249–257.
- Cronan, D.S., Glasby, G.P., Moorby, S.A., Thompson, J., Knedler, K.E., and McDougall, J.C. (1982) A submarine hydrothermal manganese deposit from the south-west Pacific Island arc. *Nature*, 298, 456–458.
- Dixon, J.B. and Skinner, H.C.W. (1992) Manganese minerals in surface environments. In H.C.W. Skinner and R.W. Fitzpatrick, Eds., *Biomineralization processes of iron and manganese—Modern and ancient environments*, p. 31–50. Catena Verlag, Cremlingen.
- Drits, V.A. (1987) Electron diffraction and high resolution electron microscopy of mineral structures, 304 p. Springer-Verlag, Berlin.
- Drits, V.A. and McCarty, D. (1996) The nature of diffraction effects from illite and illite-smectite consisting of interstratified trans-vacant and cis-vacant 2:1 layers: A semiquantitative technique for determination of layer-type content. *American Mineralogist*, 81, 852–863.

- Drits, V.A. and Tchoubar, C. (1990) X-ray diffraction by disordered lamellar structures: Theory and applications to microdivided silicates and carbons, 371 p. Springer-Verlag, Berlin.
- Drits, V.A., Petrova, V.V., and Gorshkov, A.I. (1985) Manganese minerals of Fe-Mn nodules from the sediments of the central part of Pacific Ocean and their post-sedimentation transformation. *Lithology and Raw Materials*, 3, 17–39.
- Drits, V.A., Silvester, E., Gorshkov, A.I., and Manceau, A. (1997) Structure of synthetic monoclinic Na-rich birnessite and hexagonal birnessite: I. Results from X-ray diffraction and selected-area electron diffraction. *American Mineralogist*, 82, 946–961.
- Giovanoli, R. and Arrhenius, G. (1988) Structural chemistry of marine manganese and iron minerals and synthetic model compounds. In P. Halbach, G. Friedrich, and U. von Stackelberg, Eds., *The manganese nodule belt of the Pacific Ocean: Geological environmental, nodule formation, and mining aspects*, p. 20–37. Verlag, Stuttgart.
- Giovanoli, R., Stähli, E., and Feitknecht, W. (1970a) Über Oxidhydroxide des vierwertigen Mangans mit Schichtengitter. 1. Mitteilung: Natrium-mangan(II,III)manganat(IV). *Helvetica Chimica Acta*, 53, 209–220.
- (1970b) Über Oxidhydroxide des vierwertigen Mangans mit Schichtengitter. 2. Mitteilung: Mangan(III)-manganat(IV). *Helvetica Chimica Acta*, 53, 453–464.
- Giovanoli, R., Feitknecht, W., Maurer, R., and Häni, H. (1976) Homogene Keimbildung und Keimwachstum von  $\gamma\text{MnO}_2$ . *Chimia*, 30, 268–269.
- Glover, E.D. (1977) Characterization of a marine birnessite. *American Mineralogist*, 62, 278–285.
- Gorshkov, A.I., Drits, V.A., Putilita, V.S., Pokrovskaya, E.V., and Sivtsov, A.V. (1992) Natural and synthetic birnessites. *Lithology and Raw Materials*, 6, 67–81 (in Russian).
- Kuma, K., Usui, A., Paplawsky, W., Gedulin, B., and Arrhenius, G. (1994) Crystal structures of synthetic 7 Å and 10 Å manganates substituted by mono- and divalent cations. *Mineralogical Magazine*, 58, 425–447.
- Manceau, A. and Charlet, L. (1992) X-ray absorption spectroscopic study of the sorption of Cr(III) at the oxide/water interface: I. Molecular mechanism of Cr(III) oxidation on Mn oxides. *Journal of Colloid and Interface Science*, 148, 443–458.
- Manceau, A., Gorshov, A.I., and Drits, V.A. (1992) Structural chemistry of Mn, Fe, Co, and Ni in manganese hydrous oxides: Part II. Information from EXAFS spectroscopy and electron and X-ray diffraction. *American Mineralogist*, 77, 1144–1157.
- Manceau, A., Drits, V.A., Silvester, E., Bartoli, C., and Lanson, B. (1997) Structural mechanism of  $\text{Co}^{2+}$  oxidation by the phyllosulfate busserite. *American Mineralogist*, 82, 1148–1173.
- McKenzie, R.M. (1967) The sorption of cobalt by manganese minerals in soils. *Australian Journal of Soil Research*, 5, 235–246.
- Méring, J. (1949) L'interférence des rayons-X dans les systèmes à stratification désordonnée. *Acta Crystallographica*, 2, 371–377.
- Murray, J.W. (1974) The surface chemistry of hydrous manganese dioxide. *Journal of Colloid and Interface Science*, 46, 357–371.
- Plançon, A. (1981) Diffraction by layer structures containing different kinds of layers and stacking faults. *Journal of Applied Crystallography*, 14, 300–304.
- Post, J.E. and Appleman, D.E. (1988) Chalcophanite,  $\text{ZnMn}_3\text{O}_7 \cdot 3\text{H}_2\text{O}$ : New crystal-structure determinations. *American Mineralogist*, 73, 1401–1404.
- Post, J.E. and Veblen, D.R. (1990) Crystal-structure determinations of synthetic sodium, magnesium, and potassium birnessite using TEM and the Rietveld method. *American Mineralogist*, 75, 477–489.
- Reynolds, R.C. Jr. (1989) Diffraction by small and disordered crystals. In *Mineralogical Society of America Reviews in Mineralogy*, 20, 145–181.
- Sakharov, B.A., Naumov, A.S., and Drits, V.A. (1982a) X-ray diffraction by mixed-layer structures with random distribution of stacking faults: Doklady Akademii Nauk SSSR, 265, 339–343 (in Russian).
- (1982b) X-ray intensities scattered by layer structure with short range ordering parameters  $S \geq 1$  and  $G \geq 1$ . *Doklady Akademii Nauk SSSR*, 265, 871–874 (in Russian).
- Silvester, E.J., Charlet, L., and Manceau, A. (1995) The mechanism of Cr(III) oxidation by Na-buserite. *Journal of Physical Chemistry*, 99, 16662–16669.
- Silvester, E., Manceau, A., and Drits, V.A. (1997) Structure of synthetic monoclinic Na-rich birnessite and hexagonal birnessite: II. Results from chemical studies and EXAFS spectroscopy. *American Mineralogist*, 82, 962–978.
- Stone, A.T. and Morgan, J.J. (1984) Reduction and dissolution of manganese(III) and manganese(IV) oxides by organics. 2. Survey of the reactivity of organics. *Environmental Science and Technology*, 18, 617–624.
- Stone, A.T. and Ulrich, H.J. (1989) Kinetics and reaction stoichiometry in the reductive dissolution of manganese(IV) dioxide and Co(III) oxide by hydroquinone. *Journal of Colloid and Interface Science*, 132, 509–522.
- Strobel, P., Charenton, J.C., and Lenglet, M. (1987) Structural chemistry of phyllosulfates: Experimental evidence and structural models. *Revue de Chimie Minérale*, 24, 199–220.
- Stumm, W. (1992) Chemistry of the solid-water interface: Processes at the mineral-water and particle-water interface in natural systems, 428 p. Wiley, New-York.
- Taylor, R.M., McKenzie, R.M., and Norrish, K. (1964) The mineralogy and chemistry of manganese in some Australian soils. *Australian Journal of Soil Research*, 2, 235–248.
- Usui, A. and Mita, N. (1995) Geochemistry and mineralogy of a modern busserite deposit from a hot spring in Hokkaido, Japan. *Clays and Clay Minerals*, 43, 116–127.
- Usui, A., Melline, T.A., Nohara, M., and Yuasa, M. (1989) Structural stability of marine 10 Å manganates from the Ogasawara (Bonin) Arc: Implication for low-temperature hydrothermal activity. *Marine Geology*, 86, 41–56.
- Wadsley, A.D. (1955) The crystal structure of chalcophanite,  $\text{ZnMn}_3\text{O}_7 \cdot 3\text{H}_2\text{O}$ . *Acta Crystallographica*, 8, 165–172.
- Wehrli, B., Friedl, G., and Manceau, A. (1995) Reaction rates and products of manganese oxidation at the sediment-water interface. In C.P. Huang, C. O'Melia, and J.J. Morgan, Eds., *Advances in chemistry series no. 244, Aquatic chemistry: Principles and applications of interfacial and inter-species interactions in aquatic systems*, p. 111–134. American Chemical Society of America, Washington.

MANUSCRIPT RECEIVED MARCH 19, 1997

MANUSCRIPT ACCEPTED SEPTEMBER 8, 1997